Coordinated binding of Vps4 to ESCRT-III drives membrane neck constriction during MVB vesicle formation

Manuel Alonso Y Adell,[1] Georg F. Vogel,[1,3] Mehrshad Pakdel,[1] Martin Müller,[1] Herbert Lindner,[2] Michael W. Hess,[3] and David Teis[1]

[1]Division of Cell Biology and [2]Division of Clinical Biochemistry, Biocenter; and [3]Division of Histology and Embryology; Innsbruck Medical University, Innsbruck 6020, Austria

Five endosomal sorting complexes required for transport (ESCRTs) mediate the degradation of ubiquitinated membrane proteins via multivesicular bodies (MVBs) in lysosomes. ESCRT-0, -I, and –II interact with cargo on endosomes. ESCRT-II also initiates the assembly of a ringlike ESCRT-III filament consisting of Vps20, Snf7, Vps24, and Vps2. The AAA–adenosine triphosphatase Vps4 disassembles and recycles the ESCRT-III complex, thereby terminating the ESCRT pathway. A mechanistic role for Vps4 in intraluminal vesicle (ILV) formation has been unclear. By combining yeast genetics, biochemistry, and electron tomography, we find that ESCRT-III assembly on endosomes is required to induce or stabilize the necks of growing MVB ILVs. Yet, ESCRT-III alone is not sufficient to complete ILV biogenesis. Rather, binding of Vps4 to ESCRT-III, coordinated by interactions with Vps2 and Snf7, is coupled to membrane neck constriction during ILV formation. Thus, Vps4 not only recycles ESCRT-III subunits but also cooperates with ESCRT-III to drive distinct membrane-remodeling steps, which lead to efficient membrane scission at the end of ILV biogenesis in vivo.

Introduction

The multivesicular body (MVB) pathway, cytokinesis, and viral budding use the endosomal sorting complexes required for transport (ESCRTs) for topologically equivalent membrane fission reactions (Henne et al., 2011; Schmidt and Teis, 2012). MVBs are spherical endosomes that consist of a limiting membrane and intraluminal vesicles (ILVs) that transport membrane proteins destined for degradation into lysosomes (Gruenberg and Stenmark, 2004). Five ESCRT complexes are required for the formation of ILVs and the loading of ubiquitinated membranes proteins (cargo) into growing ILVs (Raiborg and Stenmark, 2009). The sequential action of ESCRT-0, -I, and -II together with the ordered assembly of ESCRT-III links membrane invagination to cargo sorting. Membrane scission in the neck of the growing vesicle releases mature, cargo-laden ILVs into the lumen. In vivo and in vitro experiments suggest that the assembly of the ESCRT-III complex is directly involved in membrane remodeling and scission (Falguières et al., 2008; Saksena et al., 2009; Wollert et al., 2009). The mechanisms underlying this ESCRT-mediated membrane budding are not understood. The ESCRT-III complex consists of four closely related core subunits, Vps20/Chmp6, Snf7/Chmp4, Vps24/Chmp3, and Vps2/Chmp2 (Babst et al., 2002a), that share a common molecular architecture (Muziol et al., 2006). In the cytoplasm, their C termini fold back onto their core domains to maintain an autoinhibited conformation (Bajorek et al., 2009; Xiao et al., 2009). On membranes, the displacement of the C terminus triggers ESCRT-III assembly (Zamborlini et al., 2006). On endosomes, the ESCRT-II complex controls the ordered assembly of a ringlike ESCRT-III filament with a defined diameter of ∼65 nm (Babst et al., 2002b; Teis et al., 2010; Henne et al., 2012). Direct binding of the first ESCRT-III subunit Vps20 to the ESCRT-II subunit Vps25 converts Vps20 into the active nucleator

M.A. Adell and G.F. Vogel contributed equally to this paper.

Correspondence to David Teis: david.teis@i-med.ac.at

Abbreviations used in this paper: CPS, carboxypeptidase S; ESCRT, endosomal sorting complex required for transport; FLuc, Firefly luciferase; ILV, intraluminal vesicle; LUCID, luciferase reporter of intraluminal deposition; MIM, MIT-interacting motif; MIT, microtubule interacting and trafficking; MVB, multivesicular body; RLuc, Renilla luciferase; SILAC, stable isotope labeling with amino acids in cell culture; ts, temperature sensitive; WT, wild type.

The Rockefeller University Press $30.00
J. Cell Biol. Vol. 205 No. 1 33–49
www.jcb.org/cgi/doi/10.1083/jcb.201310114

for ESCRT-III assembly (Im et al., 2009; Teis et al., 2010). Vps20 then nucleates the homooligomerization of Snf7, which constitutes the major ESCRT-III subunit. ESCRT-III assembly is completed by binding of Vps24 and Vps2 (Teis et al., 2008), which also transforms ESCRT-III into spiral filaments (Henne et al., 2012). Vps2 is central for the recruitment of Vps4, which is supported by the ESCRT-III–associated protein Did2 (Babst et al., 2002a; Nickerson et al., 2006). With two other ESCRT-III–associated proteins, Ist1 and Vps60, they promote the assembly of the active Vps4 complex (Davies et al., 2010; Shestakova et al., 2010). The active Vps4 complex consists of one or two stacked hexameric rings and the cofactor Vta1, which enhances the ATPase activity and supports interactions with ESCRT-III (Azmi et al., 2006; Landsberg et al., 2009; Monroe et al., 2014). The interaction of Vps4 with ESCRT-III subunits requires its N-terminal microtubule interacting and trafficking (MIT) domain. The MIT domain consists of three antiparallel helices (Scott et al., 2005) that interact with the acidic C-terminal MIT-interacting motifs (MIMs) of the ESCRT-III subunits. One side of the MIT domain (helices α2/α3) binds to the helical MIM1 of Vps2 and Did2 and the MIM1-like element of Vps24 (Fig. 1 A; Obita et al., 2007; Stuchell-Brereton et al., 2007). The opposite side of the MIT domain (helices α1/α3) binds to the unstructured MIM2 on Vps20 and Snf7 (Fig. 1 A; Kieffer et al., 2008). This setup enables the Vps4 complex to interact with multiple MIMs exposed by fully assembled ESCRT-III, which probably enhances Vps4 activity and initiates ESCRT-III disassembly. Thereby, Vps4 recycles individual ESCRT-III subunits back to the cytoplasm, which is essential for continuous MVB sorting (Babst et al., 1997, 1998). In vitro, the ordered assembly of the ESCRT-III complex on giant unilamellar vesicles was sufficient for membrane scission (Wollert et al., 2009; Wollert and Hurley, 2010), suggesting that Vps4 has a minor if any role in membrane remodeling and only functions to recycle ESCRT-III. In vivo, Vps4 localized to HIV budding sites, before virus release (Baumgärtel et al., 2011; Jouvenet et al., 2011), and regulators of Vps4 activity influenced the size of ILVs (Nickerson et al., 2010). However, a direct function for Vps4-mediated ESCRT-III disassembly in membrane remodeling was not defined. Here, we provide evidence that the function of Vps4 in yeast extends beyond mere ESCRT-III recycling. We show that the coordinated binding of Vps4 to the ESCRT-III subunits Snf7 and Vps2 is essential for efficient membrane remodeling and neck constriction during ILV formation.

Results

Binding of Vps4 to the ESCRT-III complex is mainly mediated by Snf7 and Vps2

To understand how Vps4 functions together with ESCRT-III, we used structural information on the MIT–MIM interface to manipulate the interaction of Vps4 with the ESCRT-III complex in vivo. Therefore, we mutated specific sites in the MIMs of all ESCRT-III core subunits that have been implicated in binding to the MIT domain of Vps4 (Fig. 1 A; Obita et al., 2007; Kieffer et al., 2008; Shestakova et al., 2010). Using homologous recombination, each ESCRT-III subunit was replaced with its corresponding MIM mutant, yielding four different yeast strains: *vps20*-L188D (*vps20**), *snf7*-L199D (*snf7**), *vps24*-R218D, L219D, L222D (*vps24**), and *vps2*-L228D, K229D (*vps2**; Fig. 1 A). These mutations in Snf7, Vps24, and Vps2 did not affect the expression levels of the mutant proteins but caused them to migrate faster on an SDS-PAGE (Fig. 1 B). To test how individual MIMs contribute to the binding of Vps4 to the ESCRT-III complex, we replaced the endogenous Vps4 with a functional Vps4-HA that was immunoprecipitated from cell lysates of the MIM mutants. Mutations in the MIMs of Vps20 (*vps20**) and Vps24 (*vps24**) did not affect the binding of Vps4-HA to ESCRT-III subunits (Fig. S1 A). In the Vps2 MIM1 mutant (*vps2**), the interaction of Vps4 with all ESCRT-III subunits was reduced (Fig. 1 C, lane 4). To assess these binding defects more quantitatively, we used stable isotope labeling with amino acids in cell culture (SILAC) together with mass spectrometry. Vps4-HA was precipitated from wild-type (WT) cells (grown with heavy [$^{13}C_6$/$^{15}N_2$] L-lysine) and from *vps2** mutants. Immunoprecipitates were mixed and subjected to SDS-PAGE (Fig. S1 B). Bands containing the Vps4 and ESCRT-III complex were excised, proteolytically digested, and analyzed by mass spectrometry. MaxQuant-based quantification showed that equal amounts of Vps4-HA were isolated from WT and *vps2** mutant cells (Fig. 1 D, heavy/light ratio = 1.1; Tables S1 and S2). Vps4-HA from WT cells recovered ≥10 times more Vps24, Vps2, and the accessory ESCRT-III subunit Did2 when compared with *vps2** mutants (Fig. 1 D, heavy/light ratio > 10; Tables S1 and S2). Only heavy peptides from Snf7 and Vps20 were detected, indicating that they were only recovered from WT cells (Fig. 1 D). Mutations in the MIM2 of Snf7 (*snf7**) moderately reduced the binding of Vps4-HA to the mutant Snf7* protein (Fig. 1 C, lane 3). Unexpectedly, also less Vps24 and Vps2 was recovered from *snf7** mutants (Fig. 1 C, lane 3), indicating that the MIM2 of Snf7 helps to stabilize transient interactions of Vps4 with the ESCRT-III complex. To address how Snf7 and Vps2 contribute to the interaction of Vps4 with the membrane-associated ESCRT-III complex, we used the substrate trap mutant Vps4-E233Q. Vps4-E233Q cannot hydrolyze ATP and hence constitutively interacts with the assembled ESCRT-III complex on endosomes of WT cells as shown by subcellular fractionation (Fig. 1 E, lane 1). Similarly, in *snf7** mutants, the majority of Vps4-E233Q was membrane associated (Fig. 1 E, lane 3). In *vps2** mutants, slightly more Vps4-E233Q was detected in the cytoplasmic fraction (Fig. 1 E, lane 6). In *snf7*, vps2** double mutants, the majority of Vps4-E233Q failed to stably associate with ESCRT-III on membranes (Fig. 1 E, lane 8), indicating that Vps2 and Snf7 together mediate stable binding of Vps4 to the ESCRT-III complex. Consistently, in *snf7*, vps2** double mutants, Vps4-E233Q-HA failed to detectably coimmunoprecipitate ESCRT-III subunits (Fig. 1 F, lane 4). Immunoprecipitation of Vps4-E233Q-HA from *snf7** mutants recovered only slightly less Snf7* protein (Fig. 1 F, lane 2). Yet, in the *vps2** mutant, the interaction of Vps4-E233Q-HA with all ESCRT-III subunits was reduced (Fig. 1 F, lane 3). Corresponding mutations in the MIT domain of Vps4 that interfere with binding to either the MIM2 (I18D) or MIM1 (L64D) yielded similar results (Fig. S1 C). Collectively, these findings confirm that the interaction of Vps4 with the MIM1 of Vps2 is mainly responsible for the binding to ESCRT-III. In addition, we now show that

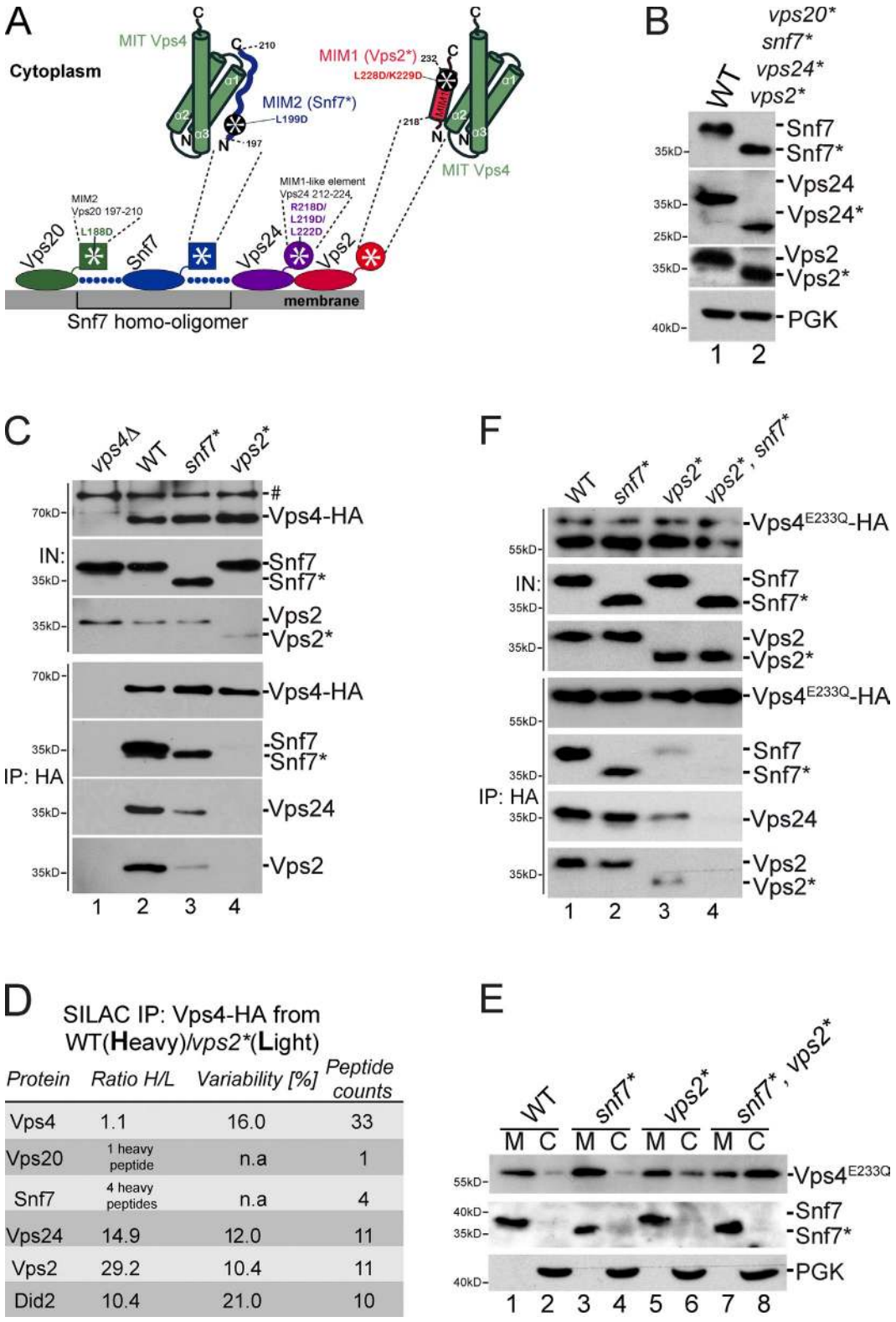

Figure 1. **Binding of Vps4 to ESCRT-III is mainly mediated by Snf7 and Vps2.** (A) The schematic representation shows ESCRT-III, the Snf7 homooligomer (blue dots), the MIM2 of Vps20 (green square), the MIM2 of Snf7 (blue square), the MIM1 of Vps24 (violet circle), the MIM1 of Vps2 (red circle), and its interaction with the MIT domain (green) of Vps4. N, N terminus; C, C terminus. (B, C, E, and F) Experiments were analyzed by SDS-PAGE and Western blotting. (B) Total cell lysates from WT cells and the *vps20*, snf7*, vps24*, vps2** quadruple mutant. (C) Immunoprecipitation (IP) of Vps4-HA from cell lysates of WT cells and the indicated mutants. #, unspecific signal. (D) Quantification (MaxQuant) of mixed Vps4-HA immunoprecipitates from WT cells (labeled with [$^{13}C_6$/$^{15}N_2$] L-lysine) and from *vps2** mutants. Heavy (H) to light (L) ratios of the ESCRT-III proteins and Vps4. Heavy/light = 1, equal peptides from WT (heavy) and *vps2** (light); heavy/light > 1, more peptides from the WT (heavy). (E) Membrane fraction (M) and cytoplasmic fraction (C) of WT cells and the indicated mutants expressing Vps4-E233Q. (F) Immunoprecipitation of Vps4-E233Q-HA from cell lysates of the indicated MIM mutants. IN, input; n.a., not annotated.

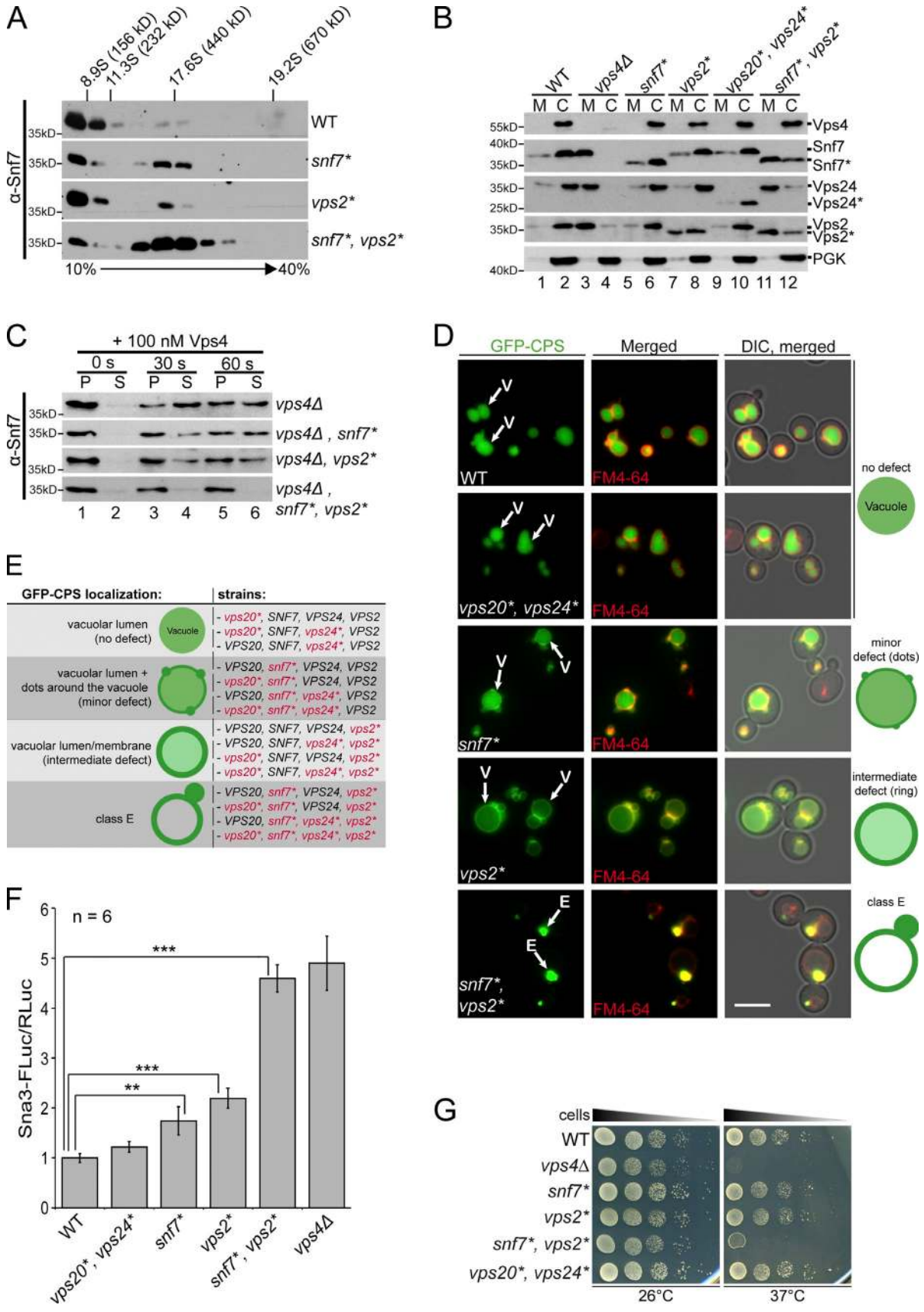

Figure 2. **The interaction of Vps4 with Snf7 and Vps2 is essential for efficient ESCRT-III disassembly and MVB sorting.** (A–C) Experiments were analyzed by SDS-PAGE and Western blotting. (A) Solubilized membrane fractions (13,000 *g* pellet) of WT cells and the indicated MIM mutants were subjected to velocity sedimentation. (B) Membrane fractions (M) and cytoplasmic fractions (C) of WT cells and the indicated mutants. (C) Semi–in vitro disassembly assay

the binding to the MIM2 of Snf7 further stabilizes Vps4 on the ESCRT-III complex.

The interaction of Vps4 with Snf7 and Vps2 is essential for efficient ESCRT-III disassembly and MVB sorting

We next addressed how the binding of Vps4 to the MIM2 of Snf7 and the MIM1 of Vps2 would affect ESCRT-III disassembly using velocity sedimentation centrifugation on 10–40% glycerol gradients. We have previously shown that membrane-associated ESCRT-III assembles into a transient higher molecular weight complex of 17.6 S, corresponding to ∼450 kD (Fig. 2 A; Teis et al., 2008). In WT cells, the majority of Snf7 was detected in low molecular weight fractions on top of the gradient. Very little of membrane-bound Snf7 was detected in the high molecular weight fraction, consistent with the transient nature of the ESCRT-III complex (Fig. 2 A). In *snf7** single mutants and *vps2** single mutants, the majority of membrane-associated Snf7 was detected in low molecular weight fractions, similar to WT cells. Yet, slightly more Snf7 was found in the high molecular weight fraction at ∼17.6 S (Fig. 2 A). In the *snf7*, vps2** double mutants, the majority of membrane-associated Snf7 was detected in a high molecular weight complex at ∼17.6 S; little Snf7 was present in low molecular weight fractions (Fig. 2 A). The size of the assembled complex was similar in all strains, suggesting that the MIM mutations did not affect ordered assembly of the ESCRT-III complex but rather compromised its disassembly and recycling, particularly in *snf7*, vps2** double mutants. Subcellular fractionation revealed that in WT cells, but also in *snf7** single mutants and in *vps20**, *vps24** double mutants, the majority of ESCRT-III was detected in the cytoplasmic fraction (Fig. 2 B). In *vps2** mutants, the subcellular distribution of Snf7 and Vps24 was not evidently affected, but more Vps2* protein was detected in the membrane fraction, suggesting incomplete ESCRT-III disassembly (Fig. 2 B, lanes 7 and 8). In the *snf7*, vps2** double mutant, all ESCRT-III subunits accumulated on membranes (Fig. 2 B, lane 11). Yet, a small fraction of Snf7* protein, Vps24, and Vps2* protein was consistently detected in the cytoplasmic fraction (Fig. 2 B, lane 12). In *vps4Δ* mutants, ESCRT-III disassembly is completely blocked; all ESCRT-III subunits accumulate on membranes and are efficiently depleted from the cytoplasm (Fig. 2 B, lanes 3 and 4). These results indicated that the reduced binding of Vps4 to the ESCRT-III complex in *snf7*, vps2** double mutants caused inefficient ESCRT-III disassembly. To assess the disassembly kinetics, we used a semi–in vitro disassembly assay (Davies et al., 2010). Addition of recombinant, purified Vps4 and ATP to membrane fractions isolated from *vps4Δ* mutants resulted in release of Snf7 from membranes into the supernatant (Fig. 2 C). Within 30 s, 100 nM Vps4 efficiently released ≥50% of Snf7 from WT membranes (Fig. 2 C, lanes 3 and 4). Mutations in the individual MIMs of Snf7 and Vps2 caused slightly slower release of Snf7 from the membrane fraction into the soluble fraction, particularly after 30 s (Fig. 2 C, lanes 3–6). Vps4-I18D or Vps4-L64D at 200 nM failed to release Snf7 from membranes (Fig. S1 D). High concentrations of Vps4-I18D (1 µM) rescued the release of Snf7 from membranes. This was not the case for Vps4-L64D, as reported previously (Fig. S1 D; Davies et al., 2010). Very little, if any, Snf7* was released from membranes isolated from *snf7*, vps2** double mutants in vitro (Fig. 2 C, lanes 3–6). Overall, these experiments suggest that individual MIM mutations cause modest delays in ESCRT-III disassembly. Simultaneous mutations of the MIMs in Snf7 and Vps2 resulted in very slow and inefficient ESCRT-III disassembly in vivo and in vitro.

To systematically address how ESCRT-III disassembly contributes to MVB sorting, we monitored the transport of GFP-tagged carboxypeptidase S (CPS) into the vacuole of all possible MIM mutant combinations (Fig. 2, D and E). None of the individual MIM mutants blocked the delivery of GFP-CPS into the vacuole (Fig. 2, D and E). *vps20** and *vps24** single mutants or *vps20*, vps24** double mutants did not show detectable MVB-sorting defects (Fig. 2, D and E; and not depicted). The transport of GFP-CPS to the lumen of the vacuole was indistinguishable from WT cells (Fig. 2, D and E). Even the deletion of the entire MIM1-like element of Vps24(1–209) did not affect GFP-CPS sorting to the vacuole (Fig. S1 E). Mutation of the MIM2 in Snf7 caused a minor defect in MVB sorting. In *snf7** mutants, the majority of GFP-CPS was transported to the vacuolar lumen, but a small fraction of GFP-CPS was missorted to the limiting vacuolar membrane and/or accumulated in vesicles around the vacuole (Fig. 2 D). *vps2** mutants displayed a more distinct MVB-sorting defect. A significant fraction of GPF-CPS reached the vacuolar lumen but also accumulated on the limiting membrane of the vacuole (Fig. 2 D). Neither *vps20*, snf7*, vps24** nor *vps20*, vps24*, vps2** triple mutants augmented the MVB-sorting defects of the respective single mutant (Fig. 2 E and Fig. S1 E). Of all possible combinations, only *snf7*, vps2** double mutants displayed a strong synthetic sorting defect; very little GFP-CPS, if any, reached the lumen of the vacuole (Fig. 2, D and E). The majority of GFP-CPS now accumulated on perivacuolar class E–like compartments, phenotypically similar to *vps4Δ* mutants. To assess the MVB-sorting defects of the MIM mutants more quantitatively, we used the luciferase reporter of intraluminal deposition (LUCID) assay (Nickerson et al., 2012). The cytoplasmic tail of the integral membrane protein Sna3 is fused to Firefly luciferase (FLuc), which is degraded via the MVB pathway. Therefore, the luciferase reporter activity is low in WT cells and approximately

with membrane fractions isolated from *vps4Δ* mutants in combination with the indicated MIM mutations. Membrane fractions were incubated with ATP and 100 nM of recombinant Vps4 for 0, 30, or 60 s. Membrane-associated proteins (13,000 *g* pellet [P]) and released proteins (13,000 *g* supernatant [S]) were separated by centrifugation. (D) Live-cell fluorescence microscopy of WT cells and the indicated mutants expressing GFP-CPS, FM4-64, vacuole (V), and the class E compartment (E). Bar, 5 µm. Schematic presentation of GFP-CPS–sorting phenotypes. DIC, differential interference contrast. (E) GFP-CPS–sorting phenotypes of all ESCRT-III MIM mutant combinations. (F) Quantification of the LUCID assay in WT cells and the indicated mutants. Ratios of the Sna3-FLuc reporter activity to the cytoplasmic Renilla luciferase (RLuc) activity normalized with SDs are shown; $n = 6$. (G) Dilution series of WT cells and the indicated mutants were grown on yeast nitrogen base plates at 26 or 37°C. **, $P < 0.01$; ***, $P < 0.001$.

fivefold increased in *vps4Δ* mutants (Fig. 2 F). The luciferase activity of *vps20*, vps24** double mutants was hardly increased when compared with WT cells (Fig. 2 F). *snf7** mutants had a 1.7-fold higher luciferase activity, and *vps2** mutants displayed twofold higher luciferase activity when compared with WT cells, consistent with partial MVB-sorting defects. *snf7*, vps2** double mutants showed an approximately fivefold increase in luciferase activity, similar to *vps4Δ* mutants (Fig. 2 F). Finally, only *snf7*, vps2** double mutants display a synthetic growth defect at a high temperature, similar to *vps4Δ* mutants (Fig. 2 G). These results demonstrate that the binding of Vps4 to the MIM1 of Vps2 and the MIM2 of Snf7 is essential for efficient ESCRT-III disassembly and MVB sorting.

Rearranging the binding of Vps4 to the ESCRT-III complex

Since the MIM2 of Snf7 and the MIM1 of Vps2 are displayed on different positions in the assembled ESCRT-III complex (Fig. 3 A), we asked whether the MIM2 and the MIM1 provide spatial information required for efficient Vps4–ESCRT-III interaction and function. We changed the positions of the MIMs by generating chimeric ESCRT-III proteins. The MIM1 (aa 214–232) of Vps2 was fused with a short linker to Vps20 (Vps20-MIM1), the first and least abundant ESCRT-III protein, and to Snf7 (Snf7-MIM1), the major ESCRT-III subunit (Fig. 3, A and B). To ensure that the properties of these chimeras are specifically mediated by the MIM1 and not caused by a defective protein folding, we generated Snf7 chimeras (Snf7-MIM1*) with an inactive MIM1 (L228D, K229D). The MIM1 of Vps2 (the last subunit that is added to the ESCRT-III complex) was replaced with the MIM2 of Snf7 (aa 197–210), yielding the chimera Vps2-MIM2. As a control, we fused the original MIM1 (aa 214–232) back onto the C terminus of Vps2-MIM2, yielding the Vps2-MIM2-MIM1 chimera (Fig. 3 B). To characterize these ESCRT-III chimeras in vitro, GST alone or GST-tagged chimeras were immobilized on beads and incubated with recombinant Vps4-E233Q and ATP. Vps4-E223Q bound weakly to GST-Snf7 and stronger to GST-Vps2 (Fig. 3 B, lanes 2 and 5) but not to GST alone (Fig. 3 B, lane 1). The GST-Snf7-MIM1 chimera, but not the GST-Snf7-MIM1* chimera, bound to Vps4-E233Q comparable to GST-Vps2 (Fig. 3 B, lanes 3 and 4). Replacing the MIM1 of Vps2 with the MIM2 of Snf7 (GST-Vps2-MIM2) reduced the binding of Vps4-E233Q, suggesting that the MIM2 of Snf7 could not replace the MIM1 (Fig. 3 B, lane 6). Readdition of the MIM1 to the Vps2-MIM2 chimera restored the strong binding of Vps4-E233Q in vitro (Fig. 3 B, lane 7). In vitro, Vps4 exhibited higher affinity for the MIM1 of Vps2 when compared with the MIM2 of Snf7.

Next, we analyzed whether Snf7-MIM1 assembled into chimeric ESCRT-III complexes on endosomes. In *vps4Δ* mutants, the chimeric ESCRT-III complexes accumulated on endosomes (Fig. S2 A, lanes 7–12). Velocity sedimentation centrifugation on 10–40% glycerol gradients showed that the majority of the Snf7-MIM1 was detected in low molecular weight fractions on top of the gradient. Very little of membrane-bound Snf7-MIM1 was detected in the high molecular weight fraction, consistent with the transient nature of the chimeric ESCRT-III complex (Fig. S2 B). In *vps4Δ* mutants, the majority of membrane-associated Snf7-MIM1 was detected in a high molecular weight complex at ∼17.6 S (Fig. S2 B). It seems that the chimeric ESCRT-III subunits assemble into membrane-bound complexes that are similar to WT–ESCRT-III complexes.

To probe the binding of Vps4 to the chimeric ESCRT-III complexes in vivo, we used immunoprecipitation. Vps4-HA recovered similar amounts of Snf7, Snf7-MIM1, and Snf7-MIM1*, suggesting that ESCRT-III interactions are primarily driven by binding to Vps2 (Fig. 3 C, lanes 1–3). However, in *vps2** mutants, the Snf7-MIM1 chimera could restore the interaction with Vps4 (Fig. 3 C, lane 5), whereas the Snf7-MIM1* chimera could not (Fig. 3 C, lane 6). Interestingly, Snf7-MIM1 also rescued the interaction of Vps4 with Vps24 but not with Vps2* (Fig. 3 C, lane 5). Deletion of the entire MIM1 from Vps2(1–214) reduced the interaction of Vps4-E233Q with ESCRT-III (Fig. 3 D, lane 2), similar to the Vps2* mutation (Fig. 1 F, lane 3). Again, the Vps2-MIM2 chimera could not restore the interaction of Vps4-E233Q with ESCRT-III (Fig. 3 D, lane 4). However, once a functional MIM1 was displayed on the ESCRT-III complex, presented either by Snf7-MIM1 or by Vps2-MIM2-MIM1, Vps4-E233Q binding to the ESCRT-III complex was restored (Fig. 3 D, lanes 3, 5, and 6). The interaction of Vps4-E233Q to Vps2(1–214) or Vps2-MIM2 always remained low (Fig. 3 D, lanes 3 and 5). Thus, the efficient interaction of Vps4 with the ESCRT-III complex requires at least one MIM1 of Vps2 and the MIM2 of Snf7 regardless of their respective positions within the assembled ESCRT-III complex. It seems that chimeric ESCRT-III subunits assemble into an ESCRT-III complex in which the interactions with Vps4 are rearranged.

The MIMs of Vps2 and Snf7 couple ESCRT-III disassembly to ILV biogenesis

Next we tested whether these rearranged Vps4–ESCRT-III interactions would support ESCRT-III disassembly and MVB sorting using subcellular fractionation and live-cell fluorescence microscopy. Expression of *SNF7*, *snf7-MIM1*, or *snf7-MIM1** complemented the MVB-sorting defect in *snf7Δ* mutants (Odorizzi et al., 1998). GFP-CPS was transported to the lumen of the vacuole indistinguishable from WT cells (Fig. 4, A [sections 1 and 2] and C). Hence, Snf7-MIM1 and Snf7-MIM1* are functional subunits that did not affect ESCRT-III assembly (Fig. S2, A and B) or disassembly in vivo. Similar results were obtained for Vps20-MIM1 (Fig. S3 B). As expected from the interaction experiments, replacing the MIM1 of Vps2 with the MIM2 (*vps2-MIM2*) displayed GFP-CPS–sorting defects similar to the *vps2** or the *vps2(1–214)* MIM1 deletion mutant (Fig. 4 A, section 3; and Fig. S3 C, sections 1 and 2). Yet, the Vps2-MIM2-MIM1 chimera fully restored ESCRT-III disassembly and MVB sorting (Fig. 4 A, section 6). Snf7-MIM1, which restored the interaction of Vps4 with ESCRT-III in a *vps2** background, was also able to mediate complete ESCRT-III dissociation from membranes in a *vps2** mutant, indistinguishable from WT cells (Fig. 4 A, section 4). All ESCRT-III proteins, including the mutant Vps2*, were released from endosomes (Fig. 4 A, compare subcellular distribution of Vps2* in sections 3 and 4). Velocity sedimentation centrifugation showed that little Snf7-MIM1

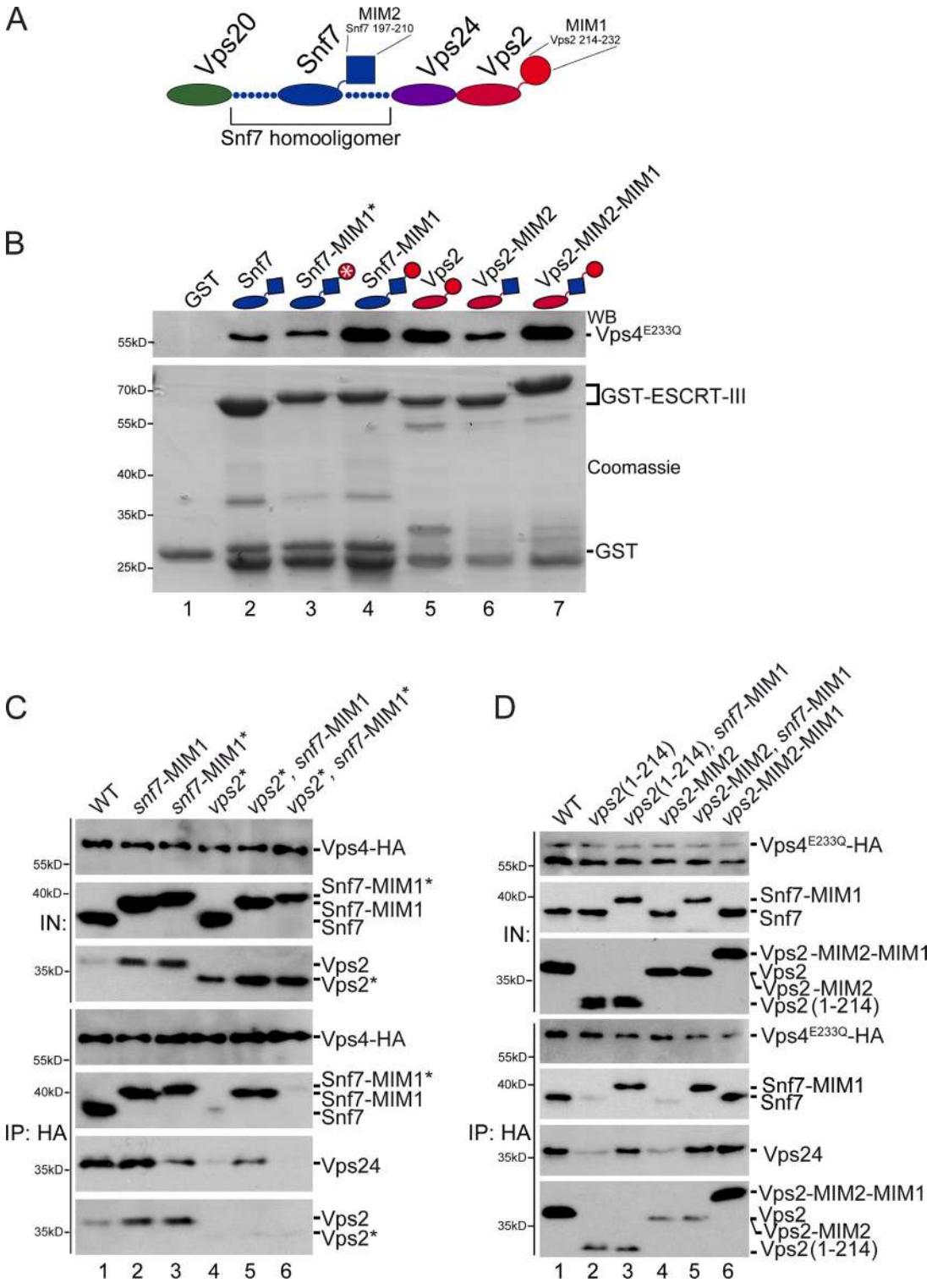

Figure 3. **Rearranging the binding of Vps4 to the ESCRT-III complex.** (A) Schematic representation of the ESCRT-III complex. (B) In vitro pull-down assay with ESCRT-III chimeras. Their domain organization is shown. GST alone or the indicated GST–ESCRT-III chimeras were immobilized on beads and incubated for 10 min at RT with Vps4-E233Q and 1 mM ATP. Bound fractions were analyzed by SDS-PAGE, Western blotting (WB), or Coomassie staining. (C and D) Vps4-HA (C) or Vps4-E233Q-HA (D) were immunoprecipitated (IP) from cell lysates of the indicated mutants and analyzed by SDS-PAGE and Western blotting. IN, input.

was detected at high molecular weight at ~17.6 S, similar to WT cells (Fig. S2 B). In contrast, Snf7-MIM1* did not restore full ESCRT-III release. Vps2* was still found on the membrane (Fig. 4 A, section 5), and slightly more Snf7-MIM1* was found in the high molecular weight fraction at ~17.6 S (Fig. S2 B). Consequently, Snf7-MIM1* did not rescue the partial MVB-sorting defects of a *vps2** mutant (Fig. 4 A, section 5). Although Snf7-MIM1 restored binding of Vps4 and ESCRT-III disassembly,

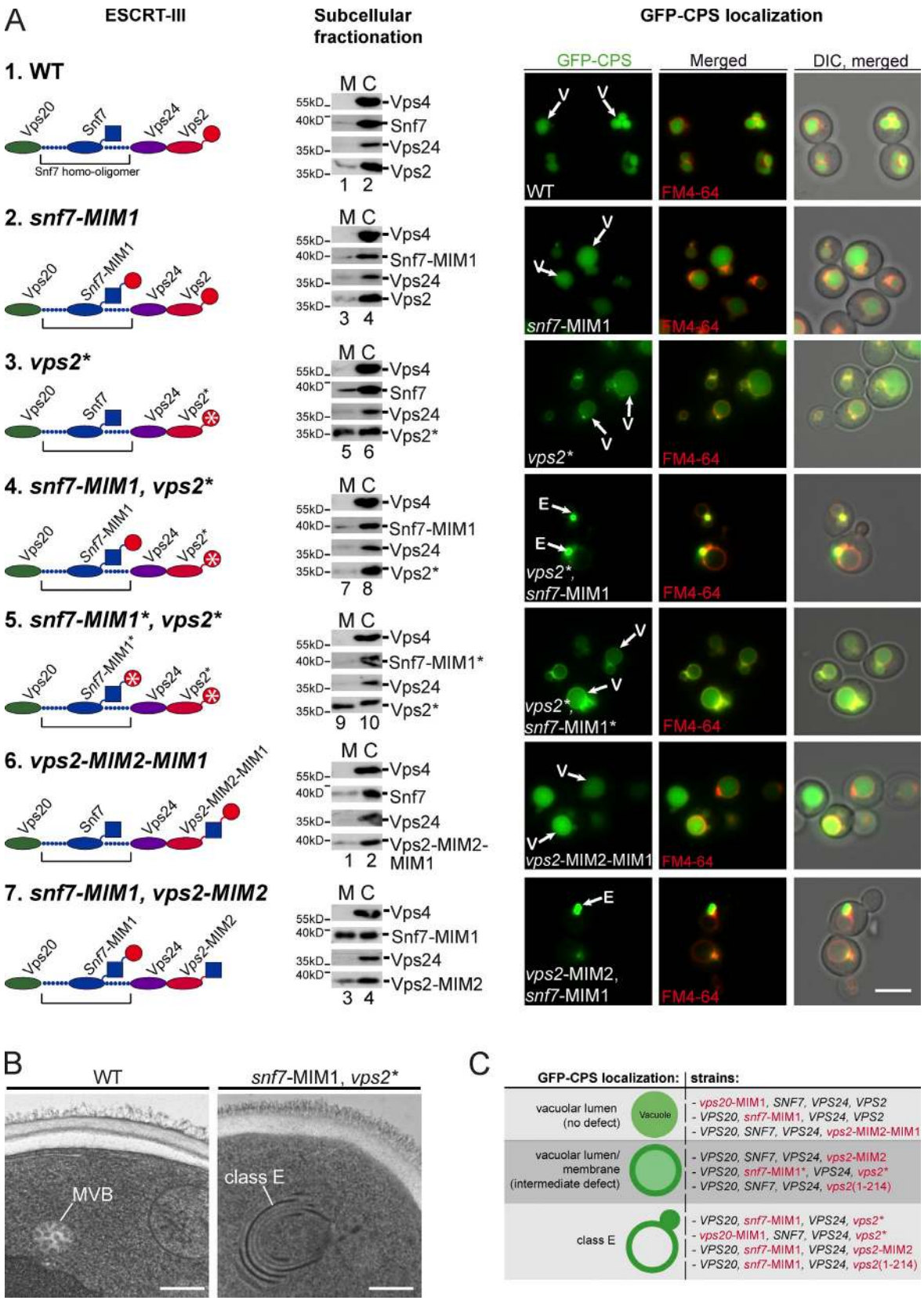

Figure 4. **The MIMs of Vps2 and Snf7 couple ESCRT-III disassembly to ILV biogenesis.** (A) Sections 1–7 show schematic representation of ESCRT-III complexes, the corresponding subcellular fractionation, and live-cell microscopy using GFP-CPS and FM4-64. Bar, 5 µM. Membrane fractions (M) and cytoplasmic fraction (C) of the indicated mutants were analyzed by SDS-PAGE and Western blotting. The uncut films are shown in Fig. S3 A. V, vacuole; E, class E compartment; DIC, differential interference contrast. (B) Transmission EM of cryofixed WT cells and *snf7*-MIM1, *vps2** mutants with class E compartments. Bar, 250 nm. (C) GFP-CPS–sorting phenotypes of the tested strains with different chimeric ESCRT-III complexes.

it failed to rescue the partial MVB-sorting defect in *vps2** mutants. Instead, Snf7-MIM1 aggravated the *vps2** phenotype, causing the accumulation of GFP-CPS in class E–like compartments (Fig. 4 A, section 4). Transmission EM of cryofixed cells demonstrated that ILV biogenesis was completely blocked. In *snf7-MIM1, vps2** mutants, class E compartments formed despite ongoing ESCRT-III assembly and disassembly (Fig. 4 B). Chimeric ESCRT-III containing Vps2-MIM2 and Snf7-MIM1 was still partially disassembled by Vps4, but MVB sorting was abrogated (Fig. 4 A, section 7). These data suggested that the function of Vps4 is not restricted to ESCRT-III recycling. Otherwise, all ESCRT-III chimeras that restore Vps4 binding and ESCRT-III disassembly should still form ILVs. Rather, it seems that the coordinated interaction of Vps4 with Snf7 and Vps2 couples ESCRT-III disassembly to ILV biogenesis. Probably, Vps4 binding to the ESCRT complex and subsequent ESCRT-III disassembly has a more direct role in ILV formation than originally anticipated.

Vps4-mediated ESCRT-III disassembly controls ILV biogenesis in vivo

To investigate how the binding of Vps4 to Snf7 and Vps2 contributes to ILV biogenesis in vivo, we used electron tomographic reconstructions and modeling of cryofixed samples (Fig. 5, A and B; and Videos 1–4). Since MVBs are not very abundant in yeast, we overexpressed the Rab5 homologue Vps21 to enrich and cluster MVBs (Markgraf et al., 2009). Vps21 overexpression did not affect the size and the morphology of ILVs. The mean ILV diameter of WT cells was 24 nm (n = 414; SD = ±4 nm; Fig. 5, A and B; and Video 1), consistent with the previously reported size of ILVs in yeast ranging around 25 nm (Nickerson et al., 2006, 2010; Wemmer et al., 2011). Similar results were obtained when we measured the diameter of ILVs that accumulated in the lumen of vacuoles of v-ATPase–deficient (*vma4Δ*) mutants (Fig. S4, E and F). On average, we detected 69 ILVs/MBV in 11 fully reconstructed MVBs (n = 11; SD = ±32; Fig. 5 C). In *snf7** mutants, the diameter of ILVs was less uniform and slightly larger when compared with WT cells (Fig. 5, A and B; and Video 2). The mean ILV diameter in *snf7** mutants was 29 nm (n = 441; SD = ±7 nm), representing a 20% increase in diameter and a 45% increase in ILV membrane surface. The total number of ILV/MVB decreased to 45 ILVs/MVB (n = 13 fully reconstructed MVBs; SD = ±20; Fig. 5 C). The defects in ILV biogenesis in the MVBs of *vps2** mutants were slightly more pronounced (Fig. 5, A and B; and Video 3). In addition, we detected in ∼25% of *vps2** mutants "failing" MVB structures, which contained few, if any, ILVs in the lumen of deformed membrane cisternae, reminiscent of class E compartments. The mean diameter of ILVs in the *vps2** mutant was 30 nm (n = 512; SD = ±8 nm), similar to *snf7** mutants. The number of ILVs/MVB was further reduced to 25 ILVs/MVB (n = 10 fully reconstructed MVBs; SD = ±14; Fig. 5 C). Vps4-I18D caused again a slightly stronger defect (Fig. S4 D). The mean diameter of ILVs was 30 nm (n = 379; SD = ±7 nm), but the number of ILVs/MVB was further reduced to 10 ILVs/MVB (n = 10 fully reconstructed MVBs; SD = ±4; Fig. 5, B and C). Vps4-L64D blocked ILV biogenesis and caused the formation of bona fide class E compartments (Fig. S4 C). Fluorescence microscopy already indicated a severe MVB-sorting defect in *snf7*, vps2** double mutants, suggesting the formation of class E compartments. The ultrastructural analysis of the *snf7*, vps2** double mutants revealed a distinct phenotype. In the majority of cells, MVBs with few but large ILVs with a mean diameter of 41 nm (n = 157; SD = ±16 nm) were detected, corresponding to a threefold increase in ILV membrane surface (Fig. 5, A and B; and Video 4). The mean number of ILV/MVB was dramatically reduced to three (n = 15 fully reconstructed MVBs; SD = ±1; Fig. 5 C). Interestingly, large ILV budding profiles were frequently observed. In some cells, class E–like structures with ILV budding profiles and few but large ILVs were observed. The phenotype of the *snf7*, vps2** double mutant was independent of Vps21 overexpression (Fig. S4, A and B).

To address whether the MVB phenotype of the *snf7*, vps2** mutant was caused by a general block in the ESCRT-III recycling or driven by slow but continuous ESCRT-III disassembly, we applied a temperature-sensitive (ts) *vps4*-ts mutant. ESCRT-III disassembly and MVB morphology are not affected in *vps4*-ts mutants that grow at the permissive temperature (26°C; Babst et al., 1998; Russell et al., 2012). Blocking *vps4*-ts function at the nonpermissive temperature (37°C) efficiently depleted cytoplasmic ESCRT-III in WT cells and *snf7*, vps2** double mutants (Fig. 6 A, lanes 1–3) and blocked ILV biogenesis. Class E compartments devoid of ILVs formed in WT cells and *snf7*, vps2** double mutants (Fig. 6 C and Fig. S5 A). Then, the same cells were shifted back to the permissive temperature (26°C) to restore the function of *vps4*-ts. Cycloheximide was added 15 min before this temperature shift to block protein synthesis (Fig. 6 B). Thereby, the recovery of ILV biogenesis became entirely dependent on the recycling of the available ESCRT-III pool in WT cells and *snf7*, vps2** double mutants. In WT cells, but not in *vps4Δ* mutants, ESCRT-III recycling (Fig. 6, lanes 4 and 7) and MVB sorting were efficiently restored (Fig. S5 A). Despite a block in protein synthesis, *snf7*, vps2** double mutants restored ESCRT-III recycling and ILV biogenesis, to the extent observed before *vps4*-ts was inactivated; a small but consistent pool of Snf7* was again detected in the cytoplasmic fraction (Fig. 6 A, lanes 6 and 9), fewer ILVs/MVB were formed (three ILVs/MVB, SD = ±2; n = 15 fully reconstructed MVBs), and the ILVs were larger (mean diameter = 39 nm, SD = ±16 nm; n = 116; Fig. 6 C).

Other ESCRT complexes were also not trapped in *snf7*, vps2** mutants but still recycled slowly (Fig. S5, B and C). In *snf7*, vps2** mutants, Vps23-GFP was detected on class E compartments but also on peripheral endosomes and in the cytoplasm, similar to WT cells. In *vps4Δ* mutants, Vps23-GFP localized almost exclusively to class E compartments and was depleted from the cytoplasm (Fig. S5, B and C). Overall, this analysis showed that mutations affecting the coordinated binding of Vps4 to ESCRT-III and subsequent disassembly/remodeling directly influence ILV biogenesis in vivo.

Binding of Vps4 to Snf7 and Vps2 is required for ILV neck constriction

To better understand which step of ILV biogenesis requires the binding of Vps4 to ESCRT-III, we carefully analyzed the budding

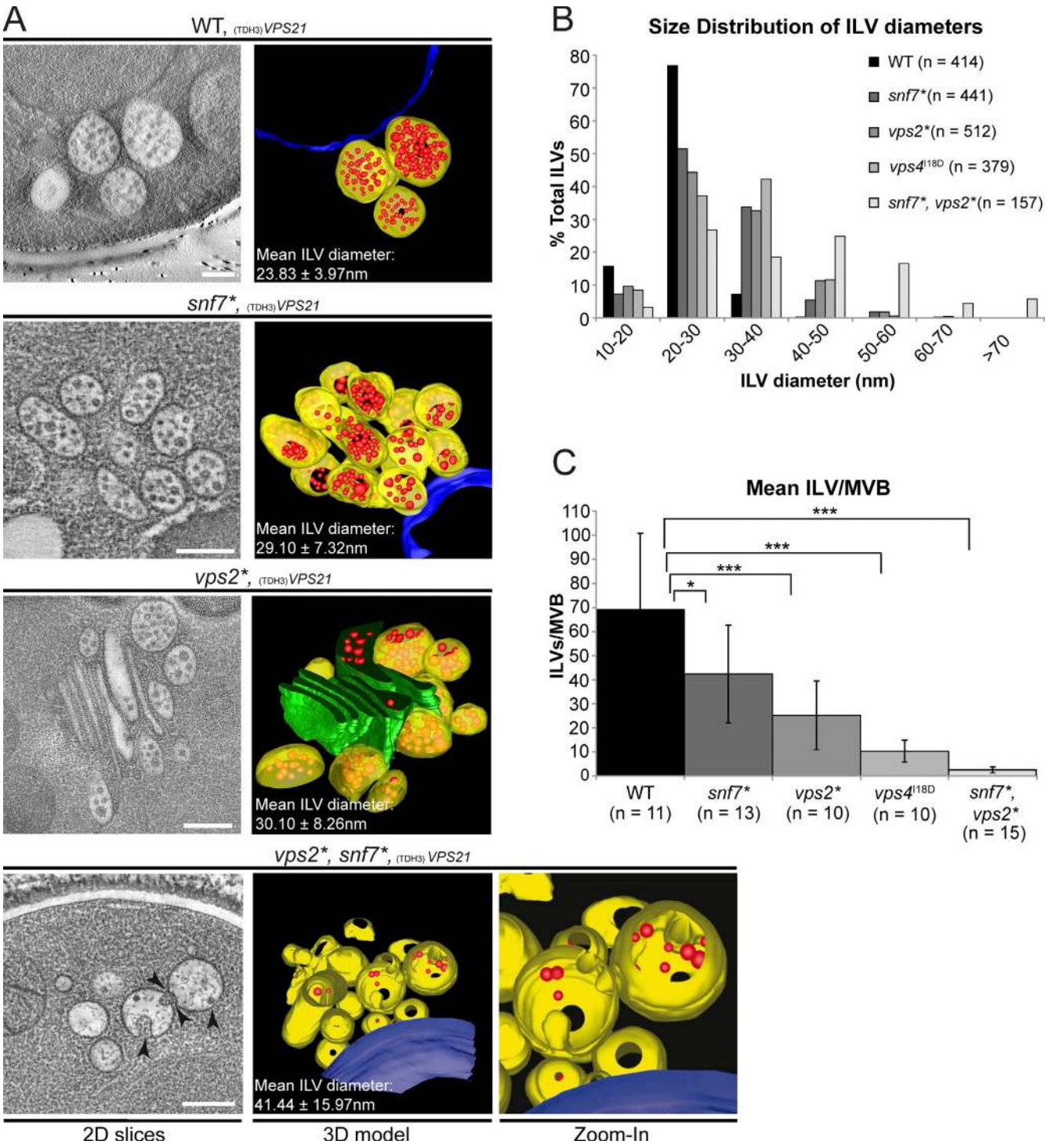

Figure 5. **Vps4-mediated ESCRT-III disassembly controls ILV biogenesis in vivo.** (A) Electron tomography of cryofixed WT cells overexpressing Vps21 (TDH3-*VPS21*) and the indicated mutants. 2D slices from tomographic reconstructions and models from 400-nm sections are shown. Limiting MVB membrane (yellow), ILVs (red), nuclear envelope (blue), and class E–like structures (green) are shown. Bars, 150 nm. Arrowheads point to enlarged budding profiles in the *snf7*, vps2** double mutants. (B) Size distribution (in 10-nm steps) of ILV diameters in WT cells and the indicated mutants. (C) Mean number of ILVs/MVB for ≥10 fully reconstructed MVBs from WT cells and the indicated mutants. Error bars indicate the SDs. *, P < 0.05; ***, P < 0.001.

profiles of growing ILVs, which are notoriously difficult to detect. In tomographic reconstructions, we observed approximately one ILV budding profile per MVB that could be subjected to morphometric analysis (Fig. 7, A and B). In WT cells, the necks of the growing buds had a mean diameter of 17 nm (n = 37, SD = ±6 nm), ranging from 5 to 35 nm (Fig. 7, B–D), consistent with previous observations (Wemmer et al., 2011). ILV neck diameters were similar in *snf7** mutants (diameter = 21 nm, SD = ±8 nm; n = 32) and in *vps2** mutants (diameter = 19 nm, SD = ±7 nm; n = 41; Fig. 6, C and D). Importantly in the *snf7*, vps2** double mutants, the mean ILV neck diameter increased to 45 nm (n = 37; SD = ±27 nm; Fig. 7, B–D). The mean number of ILV bud necks

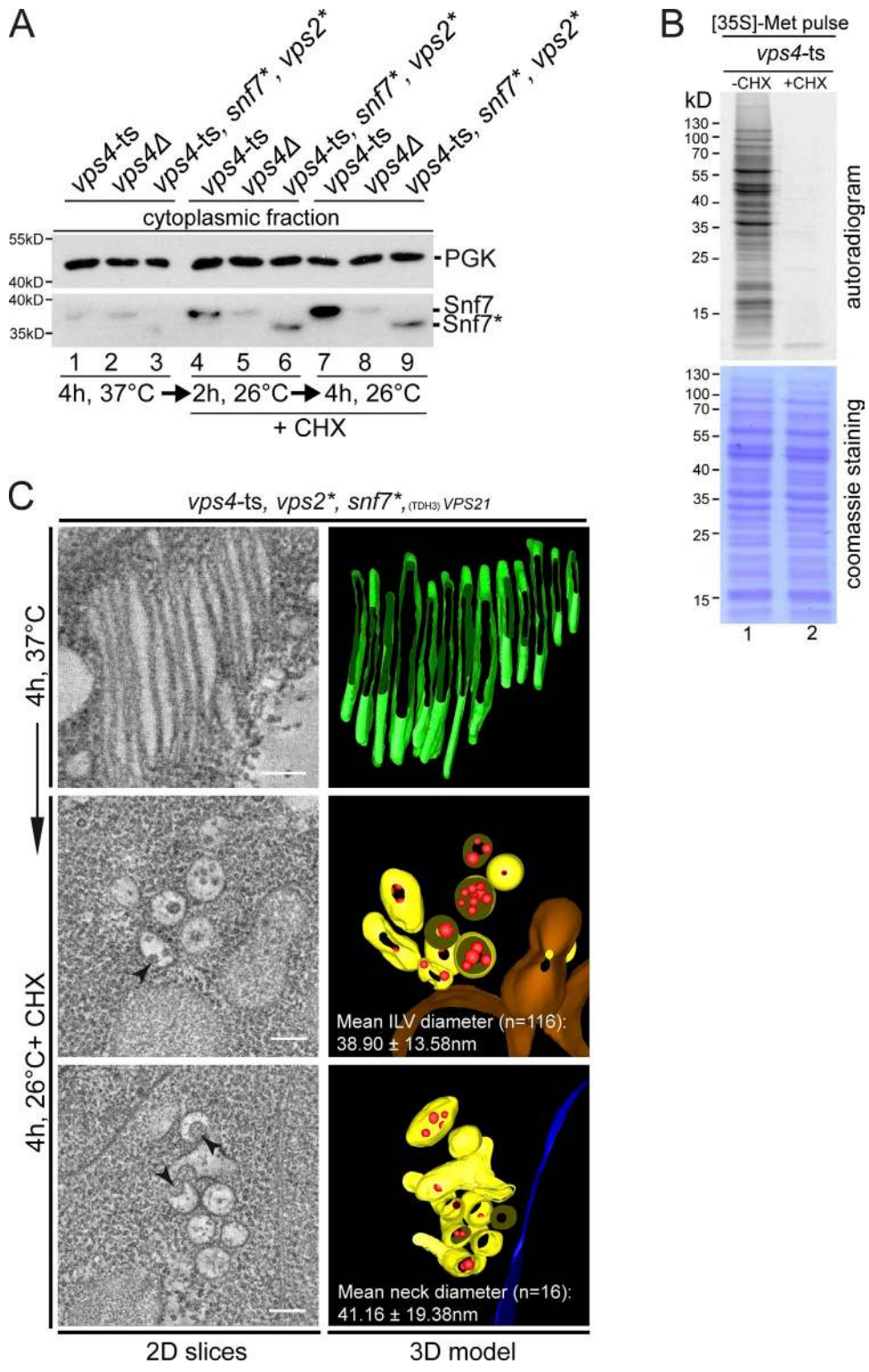

Figure 6. **Slow and continuous ESCRT-III recycling and ILV biogenesis in *snf7*, vps2** double mutants.** (A) *vps4*-ts mutants, *vps4Δ* mutants and *snf7*, vps2*, vps4*-ts mutants were shifted to the nonpermissive temperature (37°C) for 4 h. 15 min before cells were shifted back to 26°C, 50 µg/ml cycloheximide was added. Cells were incubated for 2 and 4 h at 26°C. Subcellular fractionation was performed at the indicated time points. Cytoplasmic fractions were analyzed by SDS-PAGE and Western blotting. (B) Cells were incubated with cycloheximide (CHX) and labeled for 5 min with [^{35}S]methionine. Autoradiogram and Coomassie staining of cell lysates is shown. (C) Electron tomography of cryofixed *snf7*, vps2*, vps4*-ts mutants at the indicated temperatures and times. 2D slices from tomographic reconstructions and models from 400-nm sections are shown. Arrowheads point to enlarged budding profiles. Limiting MVB membrane (yellow), ILVs (red), vacuolar membrane (brown), nuclear envelope (blue), and class E–like structures (green) are depicted. Bars, 150 nm.

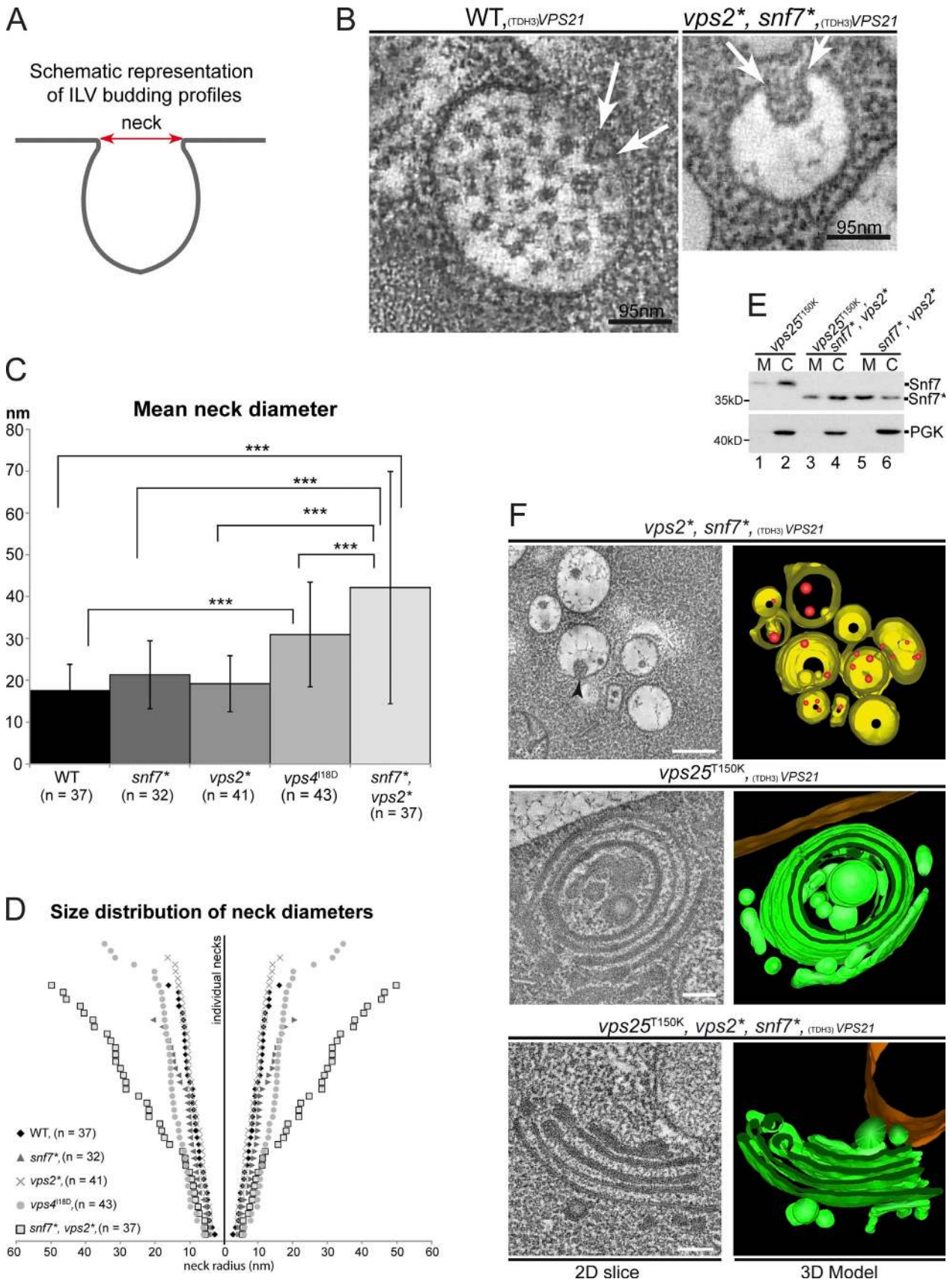

Figure 7. **Binding of Vps4 to Snf7 and Vps2 is required for ILV neck constriction.** (A) Schematic representation of ILV budding profiles as detected in tomographic reconstructions. (B) MVB of WT cells and MVB-like structure from *snf7*, vps2** double mutants. The arrows indicate ILV necks. (C) Mean membrane neck diameters measured in the tomograms. Error bars indicate the SD of the membrane neck diameters measured in the tomograms.

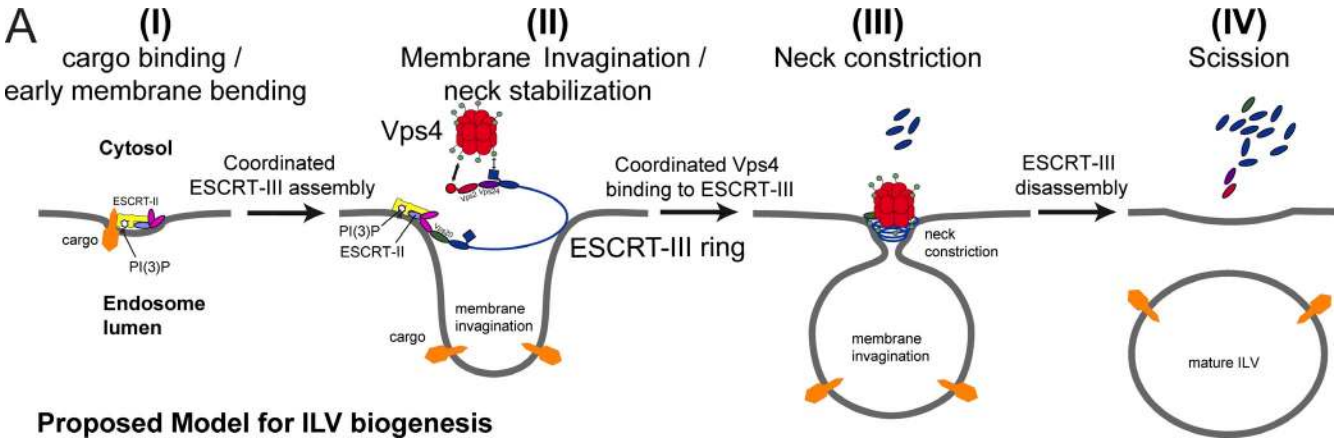

Figure 8. **Proposed model for ILV biogenesis.** PI(3)P, phosphatidylinositol 3-phosphate.

per MVB was similar in WT cells and *snf7*, vps2** mutants. In WT cells (37 bud necks on 31 MVBs) and *snf7*, vps2** mutants (37 necks on 30 MVBs), one ILV bud neck per MVB was detected on average. ILV neck diameters of 40–50 nm are remarkably consistent with the inner diameter of the ESCRT-III ring induced by ESCRT-II in vitro (Henne et al., 2012).

In *snf7*, vps2** double mutants, ESCRT-III assembled into a more stable high molecular weight complex, in size corresponding to the more transient ESCRT-III complex in WT cells (Fig. 2 A). Maybe the wider bud necks were caused by inefficient ESCRT-III disassembly, suggesting that Vps4 and ESCRT-III would function together in neck constriction. Alternatively, ESCRT-I and ESCRT-II together may already have induced these invaginations (Wollert et al., 2009; Wollert and Hurley, 2010). Yet, in the *snf7*, vps2** double mutants, these membrane necks cannot undergo scission because new ESCRT-III complexes cannot properly assemble as a result of inefficient ESCRT-III recycling. To directly address whether ESCRT-III assembly is required to induce or stabilize ILV necks in a *snf7*, vps2** double mutant, we used a single point mutation (T150K) in the ESCRT-II subunit Vps25. Vps25 binds specifically to helix α1 of Vps20 and thereby converts Vps20 into the active nucleator for ESCRT-III assembly. The T150K mutation in Vps25 specifically prevents the interaction of Vps20 with ESCRT-II, and hence, ESCRT-III no longer assembles (Im et al., 2009; Teis et al., 2010). Subcellular fractionation demonstrated that mutant ESCRT-II complexes (*vps25T150K*) reduced the accumulation of ESCRT-III in the membrane fraction of *snf7*, vps2** double mutants (Fig. 7 E, lanes 3 and 5). Hence, in *snf7*, vps2** double mutants, ESCRT-III assembly followed the canonical ESCRT-II–dependent pathway. Electron tomography showed that ESCRT-II–dependent assembly of the ESCRT-III complex was essential to induce or stabilize ILV bud necks. In a majority of *snf7*, vps2** double mutants, MVBs with large ILV bud necks and few, but large, ILVs were detected (Fig. 7 F). However, when ESCRT-III no longer efficiently assembled in ESCRT-II (*vps25-T150K*) mutants, bona fide empty class E compartments, devoid of ILV budding profiles and ILVs, were observed in the vast majority of cells (Fig. 7 F and Video 5). These findings strongly suggested that ESCRT-II–mediated assembly of the ESCRT-III complex is required to induce or stabilize ILV budding structures/necks in vivo. Yet, ESCRT-III assembly remains insufficient to complete ILV budding. It follows that efficient budding requires the coordinated binding of Vps4 to Snf7 and Vps2 in the assembled ESCRT-III complex. Thereby, the Vps4-dependent ESCRT-III disassembly reaction plays a key role in ILV biogenesis, most likely by inducing conformation changes in ESCRT-III that drive membrane deformation and bud neck constriction, which ultimately lead to membrane scission in vivo (Fig. 8).

Discussion

ESCRT-III and Vps4 are essential for all ESCRT-mediated budding reactions, and it is clear that Vps4 is required to disassemble ESCRT-III from membranes and recycle its individual subunits back into the cytoplasm (Adell and Teis, 2011). However, the role of Vps4 in ILV biogenesis was not clear. We propose here that the coordinated binding of Vps4 to Snf7 and Vps2 directly couples ESCRT-III disassembly to membrane neck constriction during MVB biogenesis (Fig. 8). The binding of Vps4 to the fully assembled ESCRT-III complex is mainly mediated by the MIM1 of Vps2 and a recruitment complex consisting of Did2 and Ist1 (Shestakova et al., 2010). The interaction of Vps4 with the MIM2 of Snf7 further stabilizes Vps4 on ESCRT-III. Binding of Vps4 to Snf7 and Vps2 could result in maximal occupancy of its MIT domains, which also stimulates the ATPase activity (Azmi et al., 2008; Merrill and Hanson, 2010; Shestakova et al., 2013). In yeast, Vta1 and Doa4 also have MIT (or MIT-like) domains and participate in the ESCRT pathway. The MIT of Vta1 binds to the MIMs in Did2 and Vps60 (Azmi et al., 2008). The MIT-like

(D) Size distribution of individual membrane neck diameters of the WT and the indicated mutants. (E) Membrane fraction (M) and cytoplasmic fraction (C) of the indicated mutants were analyzed by SDS-PAGE and Western blotting. (F) 2D slices and 3D models from 400-nm sections of the indicated mutants overexpressing Vps21 (TDH3-*VPS21*). Limiting MVB membrane (yellow), ILVs (red), vacuolar membrane (brown), and class E compartments (green) are shown. Bars, 150 nm. ***, $P < 0.001$.

domain of Doa4 binds to Vps20 (Richter et al., 2013). Our results imply that the major function of the MIM1 of Vps2 and the MIM2 of Snf7 is to coordinate the binding of Vps4 to the ESCRT-III complex. However, there are no general rules that define the interaction of MITs with MIMs (Hurley and Yang, 2008). Therefore, we cannot entirely rule out that other interactions of the MIMs of Vps2 and Snf7 are independent of Vps4 but also contribute to the ESCRT pathway.

Deletions in the C-terminal region encompassing the MIM1 of Chmp2B/Vps2 cause a rare autosomal dominant frontotemporal dementia. Patient fibroblasts contained enlarged, deformed MVBs with few ILVs (Urwin et al., 2010), somewhat reminiscent to the disturbed MVB morphology that we observe in yeast MIM mutants. We did not detect a significant role for the MIM2 of Vps20/Chmp6 or for the MIM1-like element of Vps24/Chmp3 in Vps4 binding to ESCRT-III, disassembly, or MVB sorting in yeast. Although it remains currently unclear how Vps4 disassembles the ESCRT-III complex, disassembly reactions of other AAA-ATPases with simple polymeric substrates are better characterized. Katanin and Spastin use their N-terminal MIT domain to interact with the acidic C terminus of (α/β) tubulin on microtubules and exert mechanical tugs sufficient to cause microtubule catastrophe (Roll-Mecak and Vale, 2008). The type VI secretion system of gram-negative bacteria requires the AAA-ATPase, ClpV, to disassemble large tubules of cogwheel-like VipA/VipB polymers (Bönemann et al., 2009). Interestingly, ClpV only interacts with VipB, and its removal is sufficient to drive the collapse of the VipA/VipB tubule (Pietrosiuk et al., 2011). Often, it seems to be sufficient for AAA-ATPases to extrude key subunits to disassemble or collapse polymeric substrates. Similarly, Vps4 could extract key ESCRT-III subunits to induce a catastrophic breakdown of the entire filament or processively disintegrate the ESCRT-III complex. Hence, we speculate that the coordinated binding of Vps4 to Vps2 and Snf7 induces disassembly and/or may promote conformational changes in the architecture of the ESCRT-III complex, which in turn drive membrane neck constriction and scission. Recent publications support the idea that the architecture of ESCRT-III is flexible and can be remodeled. In vivo and in vitro findings suggest that ESCRT-III proteins can assemble in differently sized rings, spirals, tubes, and domes (Ghazi-Tabatabai et al., 2008; Lata et al., 2008; Bajorek et al., 2009; Guizetti et al., 2011; Effantin et al., 2013). When ESCRT-III is bound to ESCRT-II, it assembles into a ring with a defined outer diameter of ∼60 nm, which can convert into spiral filaments (Henne et al., 2012). In vitro, Vps4 binding to Vps24-Vps2 chimeras induces ESCRT-III filament bundling (Ghazi-Tabatabai et al., 2008). In vivo, ATP hydrolysis-deficient Vps4B-E235Q converts plasma membrane–associated spiral filaments consisting of hSnf7/Chmp4 or hVps2/Chmp2B into tubes projecting out of cells (Hanson et al., 2008; Bodon et al., 2011). At some point during ESCRT-III remodeling, Chmp2/3 may form a domelike structure that could promote membrane scission (Lata et al., 2008; Fabrikant et al., 2009). During cytokinesis, long ESCRT-III–dependent 17-nm filaments spiral toward the site of membrane abscission to promote cortical constriction (Guizetti et al., 2011). Vps4-induced remodeling/breakage of these ESCRT-III filaments occurs before final abscission (Elia et al., 2012). Maybe Vps4 together with ESCRT-III constitutes a mechanochemical membrane-remodeling machinery, in some ways similar to FtsZ rings or dynamin. FtsZ and dynamin are large multidomain GTPases that power several nucleotide-driven conformational states required for membrane scission (Osawa et al., 2008; Faelber et al., 2011; Shnyrova et al., 2013). The binding of Vps4 may trigger first conformational changes in ESCRT-III and then disassembly or both, but we strongly believe that they are all mechanistically linked. The characterization of these processes as well as their precise function in membrane remodeling will require new experimental approaches.

Based on published data and our results presented here, we propose the following model for the cooperation of Vps4 and ESCRT-III during ILV biogenesis (Fig. 8). ESCRT-0, -I, and –II bind and cluster ubiquitinated cargo and may already induce initial membrane deformation. ESCRT-II, most likely bound to ubiquitinated cargo, induces the ordered assembly of the ESCRT-III complex into a ringlike filament with a diameter of ∼40–60 nm, which not only encircles MVB cargo but also defines the membrane that will be remodeled into an ILV (Teis et al., 2010; Henne et al., 2012). Once complex assembly is complete, ESCRT-III either induces or stabilizes an ∼40–60-nm neck of the growing ILV, probably supported by an N-terminal insertion motif that anchors the ESCRT-III filament to membranes (Buchkovich et al., 2013). The coordinated binding of Vps4 to the ESCRT-III complex mediates productive ESCRT-III remodeling/disassembly that induces conformational changes to convert the ESCRT-III ring into a helical spiral, which then somehow drives membrane neck constriction. Maybe Vps4 converts a relaxed ESCRT-III spiral in the neck into a constricted state and thereby transmit forces to membranes for further remodeling steps. In contrast, the interaction of Vps4 with the chimeric ESCRT-III complex may result in a destructive ESCRT-III remodeling/disassembly reaction, causing the rapid collapse of the budding intermediates. Alternatively, the coordinated binding of Vps4 to ESCRT-III may already function during the initial stages of membrane invagination as well as later during bud neck constriction, implying that Vps4 and ESCRT-III could function together in multiple steps during ILV biogenesis.

The majority of ILV necks appeared to constrict close to the limiting membrane of MVBs, suggesting that the relatively large Vps4 complex (diameter ∼14 nm; Yu et al., 2008; Hartmann et al., 2008; Landsberg et al., 2009) may have access to the actual site of the final membrane scission step. Only in very few instances, long and narrow bud necks, which would exclude Vps4, were observed. In addition, the binding of Bro1 to Snf7 may negatively regulate Vps4–ESCRT-III–driven membrane scission activity to allow Doa4-dependent cargo deubiquitination before membrane scission (Wemmer et al., 2011). Given the multiple ESCRT-III isoforms in mammals, the coordinated action of Vps4 and ESCRT-III may be more complex. Still, because of the evolutionary conservation of the ESCRT-III subunits and Vps4, membrane remodeling in higher eukaryotes could follow similar concepts. Overall, our work demonstrates for the first time that the coordinated binding of Vps4 to the ESCRT-III complex is required for efficient membrane remodeling and neck constriction during MVB vesicle formation in vivo.

Materials and methods

Antibodies and reagents

Rabbit polyclonal antisera against Vps2 were produced by immunizing rabbits (Eurogentec). 1 mg H6-Vps2, purified from *Escherichia coli*, was excised from SDS-PAGE and used for immunization. The antiserum (serum agglutination test 455 α) was purified using GST-Vps2 transferred to a polyvinylidene difluoride membrane, eluted with 100 mM glycine, pH 2.5, and diluted 1:100 for Western blotting. The specificity of the antibody was tested using recombinant proteins and yeast extracts from *vps2Δ* mutants. Monoclonal anti-HA affinity agarose was obtained from Sigma-Aldrich. The mouse monoclonal anti-HA antibody (12CA5) was a gift from L. Hengst (Biocenter, Innsbruck Medical University, Innsbruck, Austria). Rabbit polyclonal antisera against Vps4, Snf7, and Vps24 were a gift from S.D. Emr (Weill Institute for Cell and Molecular Biology, Cornell University, Ithaca, NY) and have been previously described (Babst et al., 1998). Anti-PGK (phosphoglycerate kinase 1) mouse monoclonal antibody was purchased from Invitrogen. Cycloheximide was purchased from Sigma-Aldrich.

Strains, plasmids, and DNA manipulation

Information on *Saccharomyces cerevisiae* strains, plasmids, and oligonucleotides is provided in Tables S3, S4, and S5.

Protein expression and purification

Purification of recombinant proteins was performed as previously described (Babst et al., 1998; Teis et al., 2008). Recombinant proteins were expressed in *E. Coli* C41(DE3)pLysS (Lucigen). GST-tagged proteins were purified with glutathione–Sepharose 4B (GE Healthcare), washed, and either eluted with glutathione or cleaved with thrombin. H6-tagged proteins were purified with Ni–nitrilotriacetic acid agarose, washed, and eluted with imidazole. H6-Vps2 was directly eluted with SDS sample buffer (2% SDS, 0.1 M Tris, pH 6.8, 10% glycerol, 0.01% bromophenol blue, and 5% β-mercaptoethanol).

GST pull-down assay using GST–ESCRT-III

GST pull-down assays were performed as previously described (Shestakova et al., 2010). GST–ESCRT-III subunits were bound to glutathione–Sepharose 4B (GE Healthcare), washed, and incubated with Vps4-E233Q and 1 mM ATP for 10 min at RT. Bound proteins were eluted by boiling for 5 min in SDS-PAGE sample buffer and analyzed by SDS-PAGE.

Immunoprecipitation experiments

30 OD_{600} equivalents of the yeast cells grown to mid–log phase (OD = 0.6) were lysed by bead beating in immunoprecipitation buffer (100 mM KAc, 5 mM $MgCl_2$, 0.2% NP-40, and 100 mM NaCl). Solubilized proteins were subjected to immunoprecipitation for 2 h at 4°C with 30 µl anti-HA agarose. Beads were washed four times in immunoprecipitation buffer. Bound proteins were eluted with SDS sample buffer.

Subcellular fractionation assays

Subcellular fractionation of proteins into membrane-associated pellets and soluble cytoplasmic fractions was performed as previously described (Babst et al., 1997). 30 OD_{600} equivalents of the yeast cells grown to mid–log phase (OD = 0.6) were spheroblasted and homogenized by douncing. After a clearing spin (500 *g* for 5 min), supernatants were centrifuged (15,000 *g* for 10 min) to separate heavy membranes from cytosol.

Semi–in vitro ESCRT-III disassembly assay

ESCRT-III disassembly assays were performed as previously described (Davies et al., 2010). 100 OD_{600} equivalents of the yeast cells grown to mid–log phase (OD = 0.6) were spheroblasted and homogenized by douncing in chilled lysis buffer (0.2 M sorbitol, 50 mM KOAc, 2 mM EDTA, 20 mM Hepes, pH 6.8, and protease inhibitors). After a clearing spin (500 *g* for 5 min), supernatants were centrifuged (15,000 *g* for 10 min) to separate heavy membranes from cytosol. The membrane pellet was washed in 1 ml ATPase reaction buffer (100 mM KOAc, 20 mM Hepes, pH 7.4, and 5 mM MgOAc) with 1 mM sorbitol and protease inhibitors (buffer A). The repelleted membranes were resuspended in buffer A and passed through an 18-gauge needle three times and a 30-gauge needle five times for homogenization. Homogenized membranes were stored at −80°C. 100-µl reactions containing 2 OD_{600} equivalent membranes, 100 nM purified Vps4, and an ATP regeneration system (10 mM phosphocreatine, 20 U/ml creatine phosphokinase, and 0.8 mM ATP) were incubated at 26°C for 30 and 60 s. The disassembly reaction was stopped by centrifugation, and membrane-bound and -released proteins were separated by centrifugation at 13,000 rpm at 4°C.

Fluorescence microscopy

For live-cell microscopy, cells were grown to midlog (OD_{600} = 0.6) at RT in yeast nitrogen base (fluorochromes used in this study were GFP and mCherry) and labeled with FM4-64 (Invitrogen) as previously described (Vida and Emr, 1995; Teis et al., 2008). Fluorescence microscopy was performed with a microscope (Axio Imager.M1; Carl Zeiss) and an α-Plan Fluar 100×, 1.45 NA oil objective (Carl Zeiss). Images were taken with a charge-coupled device camera (Sport Explorer; Visitron Systems). Acquisition software used was VisiView 2.0.3 (Visitron Systems). Image brightness and contrast was enhanced in the RGB channel using Photoshop CS4 Extended (version 11.0.2; Adobe).

Cryofixation, EM, and tomography

Yeast cultures (0.6 OD_{600}) were subjected to high-pressure freezing with an HMP 010 (obtained from Bal-Tec) followed by freeze substitution, epoxy resin embedding, and section poststaining essentially as described previously for plants (Hess, 2007), except that freeze-substitution media consisted of acetone plus 2.5% (vol/vol) glutaraldehyde, 2% (wt/vol) uranyl acetate, 10% vol/vol methanol, 0.05% (wt/vol) OsO_4, and 1.5% water. Thin and semithin sections (100 and 400 nm, respectively) were poststained with hot ethanolic phosphotungstic acid (0.5% wt/vol in 95% ethanol for 5 min at 60°C; Locke and Krishnan, 1971). Thin sections were viewed at 80 kV with a microscope (Philips CM120; FEI) equipped with a digital camera (Morada; Olympus). Electron tomography from 400-nm semithin sections (coated with 10-nm fiducial gold) was performed on a camera (Tecnai T20-G2; FEI) at 200 kV using a dual-tilt series. Images were recorded at a binning of 2 with a 4,000 × 4,000–pixel digital camera (Eagle; FEI) from 55 to −55° with 1° increments using Inspect3D automated tomography software (obtained from FEI). Tomograms were reconstructed and modeled using IMOD software (Kremer et al., 1996). For ILV size and ILV membrane neck analysis, single slices of reconstructed tomograms were analyzed using 3dmod. For morphometry, we analyzed >30 MVBs, >150 ILVs, and >33 ILV budding profiles per cell type in 2D slices from tomographic reconstructions from seven different WT cells, four different *snf7**, five different *vps2**, and nine different *snf7*, vps2** mutants.

Dual-luciferase reporter assay (LUCID)

Dual-luciferase assays of Sna3-FLuc trafficking to the lysosome were performed as previously described (Nickerson et al., 2012). In brief, luciferase activity of Sna3-FLuc and Renilla luciferase (RLuc) was analyzed with the dual-luciferase assay system (DLR; Promega). Cells in mid–log phase (OD = 0.6) were treated with cycloheximide (50 µg/ml final) for 30 min, harvested by centrifugation, and lysed by incubation in 500 µl lysis buffer by vortexing with glass beads at RT. 5-µl aliquots of the lysate were analyzed in 96-well plate format using a luminometer (TriStar LB941; Berthold Technologies). After background subtraction, luciferase activity of Sna3-FLuc was normalized to the activity of RLuc.

Block and recovery of MVB biogenesis in *vps4*-ts mutants

Yeast cells were grown to logarithmic phase at 26°C and then shifted to 37°C for 4 h. 50 µg/ml cycloheximide was added to the growth media 15 min before shifting them back to 26°C for 4 h. 30 OD 0.6 equivalents grown at 37°C or recovering at 26°C (with cycloheximide) were subjected to subcellular fractionation, cryofixation, and electron tomography as described in this work, except that cells grown at 37°C were also spheroblasted at 37°C.

SILAC and mass spectrometry analysis

*vps2** mutants were grown in SILAC "light" medium, and WT cells were grown in SILAC "heavy" medium containing ($^{13}C_6$/$^{15}N_2$) L-lysine (20 µg/ml; Sigma-Aldrich) for 10 generations to mid–log phase (OD_{600} = 0.6). Cells were washed once with ice-cold double-distilled H_2O and used for immunoprecipitation. Immunoprecipitated proteins from WT cells (labeled with heavy lysine) and from *vps2** mutants were eluted in SDS sample buffer (without bromophenol blue), mixed, and subjected to SDS-PAGE. Proteins were digested in gel with LysC. Peptides were analyzed using an HPLC system (UltiMate 3000 Nano-LC; Dionex) coupled to a mass spectrometer (LTQ Orbitrap XL; Thermo Fisher Scientific). MaxQuant version 1.2.0.18 with search engine Andromeda and Proteome Discoverer version 1.2.0.208 (Thermo Fisher Scientific) with search engine Mascot version 2.2.07 (Matrix Science) were used for data analysis. Raw data obtained by liquid chromatography–electrophoresis electrospray ionization–mass spectrometry were searched against the yeast protein database downloaded from http://downloads.yeastgenome.org/sequence/S288C_reference/orf_protein/.

Statistical analysis

Statistical analysis was performed using robust one-way analysis of variance (ILV diameter) and Student's *t* test, unpaired and two tailed (ILV diameter and LUCID). *, $P < 0.05$; **, $P < 0.01$; ***, $P < 0.001$.

Online supplemental material

Fig. S1 shows analysis of the MIT–MIM interaction. Fig. S2 presents subcellular fractionation and velocity sedimentation centrifugation to further characterize chimeric ESCRT-III complexes. Fig S3 shows Western blot analysis (full films from Fig. 4 A) of subcellular fractionation and GPF-CPS sorting in *vps20*-MIM1 and *vps2*-MIM2 mutants. Fig. S4 contains further analysis of MVB and ILV morphology using electron tomography of cryofixed mutants: *snf7*, vps2** double mutants without VPS21 overexpression, Vps4-MIT mutants, and in *vma4Δ* mutants. Fig. S5 shows analysis of *snf7*, vps2** double mutants. Tables S1 and S2 show the SILAC-based quantification of Vps4-HA immunoprecipitation using MaxQuant and Proteome Discoverer, respectively, and relate to Fig. 1 D. Table S3 contains all yeast strains used in this study. Table S4and plasmids used in this study. Table S5 shows primers used in this study. Video 1 shows electron tomography and 3D modeling of a cryofixed WT yeast cell overexpressing Vps21. Video 2 shows electron tomography and 3D modeling of a cryofixed *snf7** mutant overexpressing Vps21. Video 3 shows electron tomography and 3D modeling of a cryofixed *vps2** mutant overexpressing Vps21. Video 4 shows electron tomography and 3D modeling of a cryofixed *snf7*, vps2** mutant overexpressing Vps21. Video 5 shows electron tomography and 3D modeling of a cryo-fixed *snf7*, vps2*, vps25*^{T150K} mutant overexpressing Vps21. Online supplemental material is available at http://www.jcb.org/cgi/content/full/jcb.201310114/DC1. Additional data are available in the JCB DataViewer at http://dx.doi.org/10.1083/jcb.201310114.dv.

We thank G. Odorizzi for the LUCID constructs. We are grateful to S.D. Emr for yeast strains and reagents, to L.A. Huber, O. Schmidt, and C. Mattissek for comments on the manuscript, to K. Gutleben and B. Witting for EM sample preparation, and L. Kremser, S. Weys, and D. Bindreither for technical assistance.

The work was funded by the Human Frontier Science Program (CDA-00001/2010-C) and the Austrian Science Fund (Y444-B12, MCBO-W01101, and SFB021-F21) to D. Teis.

The authors declare no competing financial interests.

Submitted: 25 October 2013
Accepted: 11 March 2014

References

Adell, M.A., and D. Teis. 2011. Assembly and disassembly of the ESCRT-III membrane scission complex. *FEBS Lett.* 585:3191–3196. http://dx.doi.org/10.1016/j.febslet.2011.09.001

Azmi, I., B. Davies, C. Dimaano, J. Payne, D. Eckert, M. Babst, and D.J. Katzmann. 2006. Recycling of ESCRTs by the AAA-ATPase Vps4 is regulated by a conserved VSL region in Vta1. *J. Cell Biol.* 172:705–717. http://dx.doi.org/10.1083/jcb.200508166

Azmi, I.F., B.A. Davies, J. Xiao, M. Babst, Z. Xu, and D.J. Katzmann. 2008. ESCRT-III family members stimulate Vps4 ATPase activity directly or via Vta1. *Dev. Cell.* 14:50–61. http://dx.doi.org/10.1016/j.devcel.2007.10.021

Babst, M., T.K. Sato, L.M. Banta, and S.D. Emr. 1997. Endosomal transport function in yeast requires a novel AAA-type ATPase, Vps4p. *EMBO J.* 16:1820–1831. http://dx.doi.org/10.1093/emboj/16.8.1820

Babst, M., B. Wendland, E.J. Estepa, and S.D. Emr. 1998. The Vps4p AAA ATPase regulates membrane association of a Vps protein complex required for normal endosome function. *EMBO J.* 17:2982–2993. http://dx.doi.org/10.1093/emboj/17.11.2982

Babst, M., D.J. Katzmann, E.J. Estepa-Sabal, T. Meerloo, and S.D. Emr. 2002a. Escrt-III: an endosome-associated heterooligomeric protein complex required for mvb sorting. *Dev. Cell.* 3:271–282. http://dx.doi.org/10.1016/S1534-5807(02)00220-4

Babst, M., D.J. Katzmann, W.B. Snyder, B. Wendland, and S.D. Emr. 2002b. Endosome-associated complex, ESCRT-II, recruits transport machinery for protein sorting at the multivesicular body. *Dev. Cell.* 3:283–289. http://dx.doi.org/10.1016/S1534-5807(02)00219-8

Bajorek, M., H.L. Schubert, J. McCullough, C. Langelier, D.M. Eckert, W.M. Stubblefield, N.T. Uter, D.G. Myszka, C.P. Hill, and W.I. Sundquist. 2009. Structural basis for ESCRT-III protein autoinhibition. *Nat. Struct. Mol. Biol.* 16:754–762. http://dx.doi.org/10.1038/nsmb.1621

Baumgärtel, V., S. Ivanchenko, A. Dupont, M. Sergeev, P.W. Wiseman, H.G. Kräusslich, C. Bräuchle, B. Müller, and D.C. Lamb. 2011. Live-cell visualization of dynamics of HIV budding site interactions with an ESCRT component. *Nat. Cell Biol.* 13:469–474. http://dx.doi.org/10.1038/ncb2215

Bodon, G., R. Chassefeyre, K. Pernet-Gallay, N. Martinelli, G. Effantin, D.L. Hulsik, A. Belly, Y. Goldberg, C. Chatellard-Causse, B. Blot, et al. 2011. Charged multivesicular body protein 2B (CHMP2B) of the endosomal sorting complex required for transport-III (ESCRT-III) polymerizes into helical structures deforming the plasma membrane. *J. Biol. Chem.* 286:40276–40286. http://dx.doi.org/10.1074/jbc.M111.283671

Bönemann, G., A. Pietrosiuk, A. Diemand, H. Zentgraf, and A. Mogk. 2009. Remodelling of VipA/VipB tubules by ClpV-mediated threading is crucial for type VI protein secretion. *EMBO J.* 28:315–325. http://dx.doi.org/10.1038/emboj.2008.269

Buchkovich, N.J., W.M. Henne, S. Tang, and S.D. Emr. 2013. Essential N-terminal insertion motif anchors the ESCRT-III filament during MVB vesicle formation. *Dev. Cell.* 27:201–214. http://dx.doi.org/10.1016/j.devcel.2013.09.009

Davies, B.A., I.F. Azmi, J. Payne, A. Shestakova, B.F. Horazdovsky, M. Babst, and D.J. Katzmann. 2010. Coordination of substrate binding and ATP hydrolysis in Vps4-mediated ESCRT-III disassembly. *Mol. Biol. Cell.* 21:3396–3408. http://dx.doi.org/10.1091/mbc.E10-06-0512

Effantin, G., A. Dordor, V. Sandrin, N. Martinelli, W.I. Sundquist, G. Schoehn, and W. Weissenhorn. 2013. ESCRT-III CHMP2A and CHMP3 form variable helical polymers in vitro and act synergistically during HIV-1 budding. *Cell. Microbiol.* 15:213–226. http://dx.doi.org/10.1111/cmi.12041

Elia, N., G. Fabrikant, M.M. Kozlov, and J. Lippincott-Schwartz. 2012. Computational model of cytokinetic abscission driven by ESCRT-III polymerization and remodeling. *Biophys. J.* 102:2309–2320. http://dx.doi.org/10.1016/j.bpj.2012.04.007

Fabrikant, G., S. Lata, J.D. Riches, J.A. Briggs, W. Weissenhorn, and M.M. Kozlov. 2009. Computational model of membrane fission catalyzed by ESCRT-III. *PLOS Comput. Biol.* 5:e1000575. http://dx.doi.org/10.1371/journal.pcbi.1000575

Faelber, K., Y. Posor, S. Gao, M. Held, Y. Roske, D. Schulze, V. Haucke, F. Noé, and O. Daumke. 2011. Crystal structure of nucleotide-free dynamin. *Nature.* 477:556–560. http://dx.doi.org/10.1038/nature10369

Falguières, T., P.P. Luyet, C. Bissig, C.C. Scott, M.C. Velluz, and J. Gruenberg. 2008. In vitro budding of intralumenal vesicles into late endosomes is regulated by Alix and Tsg101. *Mol. Biol. Cell.* 19:4942–4955. http://dx.doi.org/10.1091/mbc.E08-03-0239

Ghazi-Tabatabai, S., S. Saksena, J.M. Short, A.V. Pobbati, D.B. Veprintsev, R.A. Crowther, S.D. Emr, E.H. Egelman, and R.L. Williams. 2008. Structure and disassembly of filaments formed by the ESCRT-III subunit Vps24. *Structure.* 16:1345–1356. http://dx.doi.org/10.1016/j.str.2008.06.010

Gruenberg, J., and H. Stenmark. 2004. The biogenesis of multivesicular endosomes. *Nat. Rev. Mol. Cell Biol.* 5:317–323. http://dx.doi.org/10.1038/nrm1360

Guizetti, J., L. Schermelleh, J. Mäntler, S. Maar, I. Poser, H. Leonhardt, T. Müller-Reichert, and D.W. Gerlich. 2011. Cortical constriction during abscission involves helices of ESCRT-III-dependent filaments. *Science.* 331:1616–1620. http://dx.doi.org/10.1126/science.1201847

Hanson, P.I., R. Roth, Y. Lin, and J.E. Heuser. 2008. Plasma membrane deformation by circular arrays of ESCRT-III protein filaments. *J. Cell Biol.* 180:389–402. http://dx.doi.org/10.1083/jcb.200707031

Hartmann, C., M. Chami, U. Zachariae, B.L. de Groot, A. Engel, and M.G. Grütter. 2008. Vacuolar protein sorting: two different functional states of the AAA-ATPase Vps4p. *J. Mol. Biol.* 377:352–363. http://dx.doi.org/10.1016/j.jmb.2008.01.010

Henne, W.M., N.J. Buchkovich, and S.D. Emr. 2011. The ESCRT pathway. *Dev. Cell.* 21:77–91. http://dx.doi.org/10.1016/j.devcel.2011.05.015

Henne, W.M., N.J. Buchkovich, Y. Zhao, and S.D. Emr. 2012. The endosomal sorting complex ESCRT-II mediates the assembly and architecture of ESCRT-III helices. *Cell.* 151:356–371. http://dx.doi.org/10.1016/j.cell.2012.08.039

Hess, M.W. 2007. Cryopreparation methodology for plant cell biology. *Methods Cell Biol.* 79:57–100. http://dx.doi.org/10.1016/S0091-679X(06)79003-3

Hurley, J.H., and D. Yang. 2008. MIT domainia. *Dev. Cell.* 14:6–8. http://dx.doi.org/10.1016/j.devcel.2007.12.013

Im, Y.J., T. Wollert, E. Boura, and J.H. Hurley. 2009. Structure and function of the ESCRT-II-III interface in multivesicular body biogenesis. *Dev. Cell.* 17:234–243. http://dx.doi.org/10.1016/j.devcel.2009.07.008

Jouvenet, N., M. Zhadina, P.D. Bieniasz, and S.M. Simon. 2011. Dynamics of ESCRT protein recruitment during retroviral assembly. *Nat. Cell Biol.* 13:394–401. http://dx.doi.org/10.1038/ncb2207

Kieffer, C., J.J. Skalicky, E. Morita, I. De Domenico, D.M. Ward, J. Kaplan, and W.I. Sundquist. 2008. Two distinct modes of ESCRT-III recognition are

required for VPS4 functions in lysosomal protein targeting and HIV-1 budding. *Dev. Cell*. 15:62–73. http://dx.doi.org/10.1016/j.devcel.2008.05.014

Kremer, J.R., D.N. Mastronarde, and J.R. McIntosh. 1996. Computer visualization of three-dimensional image data using IMOD. *J. Struct. Biol.* 116:71–76. http://dx.doi.org/10.1006/jsbi.1996.0013

Landsberg, M.J., P.R. Vajjhala, R. Rothnagel, A.L. Munn, and B. Hankamer. 2009. Three-dimensional structure of AAA ATPase Vps4: advancing structural insights into the mechanisms of endosomal sorting and enveloped virus budding. *Structure*. 17:427–437. http://dx.doi.org/10.1016/j.str.2008.12.020

Lata, S., G. Schoehn, A. Jain, R. Pires, J. Piehler, H.G. Gottlinger, and W. Weissenhorn. 2008. Helical structures of ESCRT-III are disassembled by VPS4. *Science*. 321:1354–1357. http://dx.doi.org/10.1126/science.1161070

Locke, M., and N. Krishnan. 1971. Hot alcoholic phosphotungstic acid and uranyl acetate as routine stains for thick and thin sections. *J. Cell Biol.* 50:550–557. http://dx.doi.org/10.1083/jcb.50.2.550

Markgraf, D.F., F. Ahnert, H. Arlt, M. Mari, K. Peplowska, N. Epp, J. Griffith, F. Reggiori, and C. Ungermann. 2009. The CORVET subunit Vps8 cooperates with the Rab5 homolog Vps21 to induce clustering of late endosomal compartments. *Mol. Biol. Cell*. 20:5276–5289. http://dx.doi.org/10.1091/mbc.E09-06-0521

Merrill, S.A., and P.I. Hanson. 2010. Activation of human VPS4A by ESCRT-III proteins reveals ability of substrates to relieve enzyme autoinhibition. *J. Biol. Chem.* 285:35428–35438. http://dx.doi.org/10.1074/jbc.M110.126318

Monroe, N., H. Han, M.D. Gonciarz, D.M. Eckert, M.A. Karren, F.G. Whitby, W.I. Sundquist, and C.P. Hill. 2014. The oligomeric state of the active Vps4 AAA ATPase. *J. Mol. Biol.* 426:510–525. http://dx.doi.org/10.1016/j.jmb.2013.09.043

Muzioł, T., E. Pineda-Molina, R.B. Ravelli, A. Zamborlini, Y. Usami, H. Göttlinger, and W. Weissenhorn. 2006. Structural basis for budding by the ESCRT-III factor CHMP3. *Dev. Cell*. 10:821–830. http://dx.doi.org/10.1016/j.devcel.2006.03.013

Nickerson, D.P., M. West, and G. Odorizzi. 2006. Did2 coordinates Vps4-mediated dissociation of ESCRT-III from endosomes. *J. Cell Biol.* 175:715–720. http://dx.doi.org/10.1083/jcb.200606113

Nickerson, D.P., M. West, R. Henry, and G. Odorizzi. 2010. Regulators of Vps4 ATPase activity at endosomes differentially influence the size and rate of formation of intralumenal vesicles. *Mol. Biol. Cell*. 21:1023–1032. http://dx.doi.org/10.1091/mbc.E09-09-0776

Nickerson, D.P., M.R. Russell, S.Y. Lo, H.C. Chapin, J.M. Milnes, and A.J. Merz. 2012. Termination of isoform-selective Vps21/Rab5 signaling at endolysosomal organelles by Msb3/Gyp3. *Traffic*. 13:1411–1428. http://dx.doi.org/10.1111/j.1600-0854.2012.01390.x

Obita, T., S. Saksena, S. Ghazi-Tabatabai, D.J. Gill, O. Perisic, S.D. Emr, and R.L. Williams. 2007. Structural basis for selective recognition of ESCRT-III by the AAA ATPase Vps4. *Nature*. 449:735–739. http://dx.doi.org/10.1038/nature06171

Odorizzi, G., M. Babst, and S.D. Emr. 1998. Fab1p PtdIns(3)P 5-kinase function essential for protein sorting in the multivesicular body. *Cell*. 95:847–858. http://dx.doi.org/10.1016/S0092-8674(00)81707-9

Osawa, M., D.E. Anderson, and H.P. Erickson. 2008. Reconstitution of contractile FtsZ rings in liposomes. *Science*. 320:792–794. http://dx.doi.org/10.1126/science.1154520

Pietrosiuk, A., E.D. Lenherr, S. Falk, G. Bönemann, J. Kopp, H. Zentgraf, I. Sinning, and A. Mogk. 2011. Molecular basis for the unique role of the AAA+ chaperone ClpV in type VI protein secretion. *J. Biol. Chem.* 286:30010–30021. http://dx.doi.org/10.1074/jbc.M111.253377

Raiborg, C., and H. Stenmark. 2009. The ESCRT machinery in endosomal sorting of ubiquitylated membrane proteins. *Nature*. 458:445–452. http://dx.doi.org/10.1038/nature07961

Richter, C.M., M. West, and G. Odorizzi. 2013. Doa4 function in ILV budding is restricted through its interaction with the Vps20 subunit of ESCRT-III. *J. Cell Sci.* 126:1881–1890. http://dx.doi.org/10.1242/jcs.122499

Roll-Mecak, A., and R.D. Vale. 2008. Structural basis of microtubule severing by the hereditary spastic paraplegia protein spastin. *Nature*. 451:363–367. http://dx.doi.org/10.1038/nature06482

Russell, M.R., T. Shideler, D.P. Nickerson, M. West, and G. Odorizzi. 2012. Class E compartments form in response to ESCRT dysfunction in yeast due to hyperactivity of the Vps21 Rab GTPase. *J. Cell Sci.* 125:5208–5220. http://dx.doi.org/10.1242/jcs.111310

Saksena, S., J. Wahlman, D. Teis, A.E. Johnson, and S.D. Emr. 2009. Functional reconstitution of ESCRT-III assembly and disassembly. *Cell*. 136:97–109. http://dx.doi.org/10.1016/j.cell.2008.11.013

Schmidt, O., and D. Teis. 2012. The ESCRT machinery. *Curr. Biol.* 22:R116–R120. http://dx.doi.org/10.1016/j.cub.2012.01.028

Scott, A., J. Gaspar, M.D. Stuchell-Brereton, S.L. Alam, J.J. Skalicky, and W.I. Sundquist. 2005. Structure and ESCRT-III protein interactions of the MIT domain of human VPS4A. *Proc. Natl. Acad. Sci. USA*. 102:13813–13818. http://dx.doi.org/10.1073/pnas.0502165102

Shestakova, A., A. Hanono, S. Drosner, M. Curtiss, B.A. Davies, D.J. Katzmann, and M. Babst. 2010. Assembly of the AAA ATPase Vps4 on ESCRT-III. *Mol. Biol. Cell*. 21:1059–1071. http://dx.doi.org/10.1091/mbc.E09-07-0572

Shestakova, A., M. Curtiss, B.A. Davies, D.J. Katzmann, and M. Babst. 2013. The linker region plays a regulatory role in assembly and activity of the Vps4 AAA ATPase. *J. Biol. Chem.* 288:26810–26819. http://dx.doi.org/10.1074/jbc.M113.497032

Shnyrova, A.V., P.V. Bashkirov, S.A. Akimov, T.J. Pucadyil, J. Zimmerberg, S.L. Schmid, and V.A. Frolov. 2013. Geometric catalysis of membrane fission driven by flexible dynamin rings. *Science*. 339:1433–1436. http://dx.doi.org/10.1126/science.1233920

Stuchell-Brereton, M.D., J.J. Skalicky, C. Kieffer, M.A. Karren, S. Ghaffarian, and W.I. Sundquist. 2007. ESCRT-III recognition by VPS4 ATPases. *Nature*. 449:740–744. http://dx.doi.org/10.1038/nature06172

Teis, D., S. Saksena, and S.D. Emr. 2008. Ordered assembly of the ESCRT-III complex on endosomes is required to sequester cargo during MVB formation. *Dev. Cell*. 15:578–589. http://dx.doi.org/10.1016/j.devcel.2008.08.013

Teis, D., S. Saksena, B.L. Judson, and S.D. Emr. 2010. ESCRT-II coordinates the assembly of ESCRT-III filaments for cargo sorting and multivesicular body vesicle formation. *EMBO J.* 29:871–883. http://dx.doi.org/10.1038/emboj.2009.408

Urwin, H., A. Authier, J.E. Nielsen, D. Metcalf, C. Powell, K. Froud, D.S. Malcolm, I. Holm, P. Johannsen, J. Brown, et al.; FReJA Consortium. 2010. Disruption of endocytic trafficking in frontotemporal dementia with CHMP2B mutations. *Hum. Mol. Genet.* 19:2228–2238. http://dx.doi.org/10.1093/hmg/ddq100

Vida, T.A., and S.D. Emr. 1995. A new vital stain for visualizing vacuolar membrane dynamics and endocytosis in yeast. *J. Cell Biol.* 128:779–792. http://dx.doi.org/10.1083/jcb.128.5.779

Wemmer, M., I. Azmi, M. West, B. Davies, D. Katzmann, and G. Odorizzi. 2011. Bro1 binding to Snf7 regulates ESCRT-III membrane scission activity in yeast. *J. Cell Biol.* 192:295–306. http://dx.doi.org/10.1083/jcb.201007018

Wollert, T., and J.H. Hurley. 2010. Molecular mechanism of multivesicular body biogenesis by ESCRT complexes. *Nature*. 464:864–869. http://dx.doi.org/10.1038/nature08849

Wollert, T., C. Wunder, J. Lippincott-Schwartz, and J.H. Hurley. 2009. Membrane scission by the ESCRT-III complex. *Nature*. 458:172–177. http://dx.doi.org/10.1038/nature07836

Xiao, J., X.W. Chen, B.A. Davies, A.R. Saltiel, D.J. Katzmann, and Z. Xu. 2009. Structural basis of Ist1 function and Ist1-Did2 interaction in the multivesicular body pathway and cytokinesis. *Mol. Biol. Cell*. 20:3514–3524. http://dx.doi.org/10.1091/mbc.E09-05-0403

Yu, Z., M.D. Gonciarz, W.I. Sundquist, C.P. Hill, and G.J. Jensen. 2008. Cryo-EM structure of dodecameric Vps4p and its 2:1 complex with Vta1p. *J. Mol. Biol.* 377:364–377. http://dx.doi.org/10.1016/j.jmb.2008.01.009

Zamborlini, A., Y. Usami, S.R. Radoshitzky, E. Popova, G. Palu, and H. Göttlinger. 2006. Release of autoinhibition converts ESCRT-III components into potent inhibitors of HIV-1 budding. *Proc. Natl. Acad. Sci. USA*. 103:19140–19145. http://dx.doi.org/10.1073/pnas.0603788103